The Mid-Cell Cytoplasmic Solution to Gel State Transition Drives Cytoplasmic Mixing of Tracer Beads and Organelles in the Giant Amoebozoa Chaos carolinensis

by
Ulises Diaz

DISSERTATION
Submitted in partial satisfaction of the requirements for degree of
DOCTOR OF PHILOSOPHY

in

Biochemistry and Molecular Biology

in the

GRADUATE DIVISION
of the
UNIVERSITY OF CALIFORNIA, SAN FRANCISCO

Approved:

DocuSigned by:
Roland Mullins
E4FB70A20A7546F...

Roland Mullins
Chair

DocuSigned by:
Wallace Marshall

Wallace Marshall

DocuSigned by:
Jeremy Reiter
F07C889D1B164B3...

Jeremy Reiter

Committee Members

Anything worth doing is worth doing at 110%

The Mid-Cell Cytoplasmic Solution to Gel State Transition Drives Cytoplasmic Mixing of Tracer Beads and Organelles in the Giant Amoebozoa Chaos carolinensis

By: Ulises Diaz

ABSTRACT

The cytoplasm is a dynamic fluid where cellular building blocks and components are continuously mixing. Cytoplasmic mixing is important for transporting intracellular material ranging from nucleotides and proteins to full organelles. In large cell types, such as ameboid and neutrophil cells, cytoplasmic streaming is coupled to membrane deformations that accompany in motility. How well or how long it takes for material to mix in cytoplasmic streams during motility remains an open question. In relatively small volumes of viscous fluids at very low Reynolds numbers, such as the cytoplasm, it should be difficult to obtain significant mixing for structures in the size range of organelles simply from streaming laminar flows. Although small things like proteins can eventually mix through diffusion, microscale structures are expected to mix on a significantly slower time frame or not at all. In this work we discovered how the giant amoeba *Chaos carolinensis* overcomes these limitations using a novel cytoplasmic gel state capture and release strategy to facilitate the extremely efficient mixing of its cytoplasm. While it was previously thought that the amoeba solution to gel state transitions only occurs at the trailing and leading edge of the cell body, our work indicates that these transitions occur frequently throughout the mid-cell region, driving the cytoplasmic mixing of beads and organelles. These results indicate that amoeba reaches a stable mixed state during motility in as little as one cytoplasmic stream/flow cycle, effectively making it a Bernoulli system and thus one of the fastest possible known intracellular mixers.

To study cytoplasmic streams, we microinjected fluorescent beads into amoeba and recorded their movement using time-lapse microscopy for up to 12 hours. In addition to bead trajectories, we microinject histone H1 labeled with alexa 488 and tracked nuclei movement. To

separate the movements of beads and nuclei from overall cell motility, we employed automated image processing to stabilize the videos, making the amoeba appear to crawl in place. Power law fits of interparticle distance over time allowed us to classify bead pair separation events into sub-diffusive, diffusive, super-diffusive, and ballistic transport regimes. Using mean squared displacement analysis, we also distinguished gel-state from liquid-state flows. This classification enabled us to calculate diffusion coefficients, mean velocities, and dwell times for each state, which we used to simulate the time required for two particle populations to achieve stable mixing. To validate these simulations, we developed a method to computationally label and track two distinct bead populations from a single-color bead injection. This approach allowed us to observe new mixing events frame by frame and showed strong agreement between simulated and experimental results.

Here we show the innovative strategy through which the giant amoeba *Chaos carolinensis* achieves efficient cytoplasmic mixing despite its reliance on low-Reynolds-number, laminar flow. Our results highlight the role of mid-cell sol-to-gel transitions in facilitating efficient mixing, enabling material exchange between cytoplasmic layers and allowing complete intracellular mixing within a single flow cycle. Novel computational approaches validated the robustness of these dynamics through simulation, showing alignment with experimental data for both bead and nuclear trajectories. Moreover, pseudopod modulation was found to have minimal impact on mixing efficiency, underscoring the unique contribution of sol-to-gel state dynamics. This work establishes a robust framework for studying intracellular mixing, with potential applications across cellular systems characterized by cytoplasmic streaming.

TABLE OF CONTENTS

LIST OF FIGURES

LIST OF TABLES

LIST OF ABBREVIATIONS

MSD – Mean Squared Displacement

SMI – Subdomain Mixing Index

SNN – Simple Nearest Neighbor

PDF – Probability Density Function

PIV – Particle Image Velocimetry

Q-Q - quantile-quantile

LatB – Latrunculin B

YG – Yellow-Green (fluorescent beads)

DEM – Digital Experimental Mixing

Exp. – experiment

ER – Endoplasmic Reticulum

T0 – Time Zero

sol – solution

Sup – Supplementary

Fig - Figure

LIST OF SYMBOLS

Σ – Represents "the sum of"

μm – Micrometer (unit of length)

D – Diffusion coefficient

V – Mean velocity

s – seconds

LIST OF SUPPLEMENTARY FIGURES

CHAPTER 1

INTRODUCTION

Importance of Mixing

The cytoplasm is a densely packed environment, where diffusion alone is often insufficient for distributing macromolecules and organelles. This limitation arises due to the crowded nature of the cytoplasm, filled with proteins, organelles, and various molecular structures that significantly hinder the movement of particles. In cells diffusion is unreliable for long-distance transport [1]. To overcome this limitation, cells have evolved mechanisms to locally synthesize or secrete molecules using strategically localized organelles. This is most evident in the development of reticulated organelle networks, such as the endoplasmic reticulum (ER) and mitochondrial network, which are coordinated in conjunction to the cytoskeleton. Intracellular material is also transported using these networks by various means including, motor proteins which bind cargo and walk along these networks, anchored motor proteins which generate cytoplasmic flow, or by directly tethering material onto the network then using its growth and regulation for distribution.

In cells lacking connected organelle networks, Intracellular materials are typically transported through cytoplasmic flows, either directly through the active generation of flow or passively via diffusion and advection. In particular, larger cells have developed active mechanisms to facilitate transport through bulk cytoplasmic streaming. In these cells cytoplasmic streams are generated primarily through two mechanisms: stationary cortical motor proteins that drive cytoplasmic flow or through cellular deformation that generates cytoplasmic flow through movement of the cell boundary [2, 3].

Large, stationary cells, such as the syncytial *Drosophila* embryo before gastrulation and plant cells, rely on stationary motor proteins to drive cytoplasmic streaming [2]. In contrast, motile cells like neutrophils and giant amoebas create cytoplasmic streams through active membrane deformations that accompany cellular motility [3]. In amoeboid cells, mixing is particularly important

as these cells lack reticulated organelle networks [4] to facilitate localized delivery via targeted secretion, synthesis, or the use of molecular motors to transport cargo along these networks. However, it is unclear how effectively ameboid cells mix their intracellular material, given that cytoplasmic streams tend to be laminar in flow, which is typically insufficient for mixing at such low Reynolds numbers, such as those found in the cytoplasm.

The Reynolds number (Re) is a key dimensionless parameter in fluid mechanics that helps predict whether a fluid flow will be laminar or turbulent. It represents the ratio of inertial forces to viscous forces, providing insight into how smoothly or chaotically fluid will flow under specific conditions [5, 6, 7, 8] . The Reynolds number is given by:

$$\mathrm{Re} = \frac{\rho U L}{\mu}$$

where:

- Re is the Reynolds number,
- ρ is the fluid density,
- U is the characteristic flow velocity,
- L is the characteristic length,
- μ is the dynamic viscosity.

The cytoplasm is an environment with an extremely low Re. For instance, the Re for a 10 μm C. elegans pronucleus moving at 0.1 μm/s through the cytoplasm is reported to be as low as (10^{-9}).[9] Such a low Re indicates that the flow is highly laminar, with very little turbulence to promote mixing. Similarly, our calculations show that the ~20 μm diameter nuclei of the amoeba Chaos *carolinensis*, traveling at 10. μm/s, has a Re of approximately (10^{-7}), also within the laminar flow regime. At such a low Re, diffusion is insufficient for transporting organelles across long distances. Even the smallest organelles, like peroxisomes which range between 0.1 and 1um [10], have difficulty moving short distances within a reasonable amount of time. For example, in the hypha of the fungus Ustilago *maydis,* it is calculated that peroxisomes, measured to have a

diameter of ~0.23 μm, would take roughly 42 minutes to travel 25 μm through the cytoplasm using diffusion alone [11]. Similarly in BS-C-1 mammalian cells it is reported that an increase in lysosome size from 0.52 μm to 1.3 μm results in a decrease in lysosome diffusion coefficients [12], reflecting the effects of the size on diffusion at such low Re environments. A summary of Re regimes and mixing characteristics can be found in **table 1** (below).

Table 1: Reynolds Number and Mixing Characteristics
This table provides an overview of flow regimes based on Reynolds number ranges, along with their associated mixing characteristics. Lower Reynolds numbers correspond to laminar flow with minimal mixing, where fluid layers slide past each other smoothly. As the Reynolds number increases, transitional flow begins, introducing minor vortices. Further increases lead to transitional to turbulent flow, where mixing becomes more chaotic and involves larger vortices. At high Reynolds numbers, fully turbulent flow occurs, Characterized by intense mixing and effective blending due to widely distributed energy and eddies.

Table 1: Reynolds Number and Mixing Characteristics

Reynolds Number (Re)	Regime	Mixing Characteristics
$\mathrm{Re} < 10$	Laminar Flow	Minimal mixing; fluid layers slide smoothly past each other.
$10 \leq \mathrm{Re} < 2000$	Transitional Flow	Some degree of mixing due to instabilities; minor vortices may form.
$2000 \leq \mathrm{Re} < 4000$	Transitional to Turbulent	Increasingly chaotic mixing with larger vortices and irregular patterns.
$\mathrm{Re} > 4000$	Turbulent Flow	Intense mixing; energy is distributed widely, creating eddies and effective blending.

In large cells, like the amoeba Chaos, which can grow up to 5mm long, it's clear that diffusion alone would not be sufficient for transporting large organelles like nuclei across such long distances, especially given their size. In the Chaos genus, nuclei size ranges from 19 μm in the Chaos *carolinensis* [13] (used in this study), to 25.7 μm in Chaos *neos* [14], to 34.3 μm in Chaos diffluens [14], and 55.8 μm in Chaos *nitida* [14]. To transport such large organelles across seemingly vast distances, amoeba Chaos uses membrane deformations to create advection and enhance diffusion, allowing for long distance transport of material within a reasonable time scale. To probe the contributions of advection vs. diffusion on intracellular transport we use the Péclet number.

The Péclet number (Pe) quantifies the balance between advection and diffusion for an object moving at velocity *U* over a length *L*, with *D* as the diffusion coefficient. The Pe is given by:

$$\mathrm{Pe} = \frac{UL}{D}$$

where:

- U is the characteristic velocity of the fluid,
- L is the characteristic length over which transport occurs,
- D is the diffusion coefficient (or diffusivity) of the substance in the fluid.

The Re and Pe both describe fluid flow dynamics, with Re comparing inertial to viscous forces and Pe comparing advection to diffusion rates. While the Re predicts flow types (laminar vs. turbulent), the Pe focuses on the balance between transport mechanisms across length scales. Larger length scales favor advection, explaining the occurrence of cytoplasmic streaming in large cells. However, effective intracellular mixing likely requires additional complex flows, as seen in active turbulence, which enhances dispersion [9]. From our experimental nuclei trajectories in amoeba Chaos *carolinensis*, we estimate that the Pe in cytoplasmic streams is 77.69, which is characteristic of a weak advection system and unlikely to generate the turbulent flow necessary for efficient mixing [15]. Advection doesn't take over until after the Pe > 100, with diffusion having minimal impact at this regime. Diffusion becomes negligible when Pe >> 1000, as strong advection dominates [16,17] (**Table 2**).

Table 2: Péclet Number and Transport Characteristics
This table categorizes transport processes based on the Péclet number (Pe) highlighting the balance between diffusion and advection. Low Pe values indicate diffusion-dominated transport, where particles spread primarily through molecular diffusion. At Pe ≈ 1, advection and diffusion contribute equally. Higher Pe values, especially above 1000, show advection-dominated transport, typical in fast-moving flows like rivers and pipelines.

Table 2: Péclet Number and Transport Characteristics

Péclet Number (Pe)	Characteristic	Description
$Pe \ll 1$	Diffusion-Dominated	Transport primarily occurs due to diffusion; particles spread uniformly without significant movement by the flow. Common in stagnant or slow-moving fluids.
$Pe \approx 1$	Balanced Advection and Diffusion	Both advection and diffusion contribute equally to transport, resulting in moderate spreading influenced by both mechanisms.
$1 < Pe < 100$	Weak Advection-Dominated	Advection begins to dominate but diffusion still plays a role. Typical in slow to moderate flows with mixed spreading and bulk transport.
$100 \leq Pe \leq 1000$	Advection-Dominated	Transport is largely due to flow, with diffusion having a minimal impact. Common in rivers, streams, and pipelines.
$Pe \gg 1000$	Strong Advection-Dominated	Advection overwhelmingly dominates transport, with negligible diffusion. Found in fast-flow systems such as turbulent flows and high-speed pipelines.

Traditional View of Sol to Gel Transition

The first observations of protoplasm, consisting of the gel ectoplasm and solution endoplasm (cytoplasmic stream), were made by Eckler in 1849 [18]. However, it wasn't until 1917 that Hyman proposed the sol-gel theory [19]. The sol-gel theory explains how amoeba control their movement and shape changes using the transformation between two states of their cytoplasm. This idea was further advanced by Mast in a series of works in 1926, 1931, and 1934 [20,21.22]. Since then, modern studies have continued to focus on the sol to gel transition [23,24]. Since the sol to gel transition zone is not directly visible using light microscopy, most studies of the sol to gel transition have concentrated on the leading edge of the cell, where the solution state of the cytoplasm transitions into a gel state as the pseudopod extends, and at the rear of the cell, where the gel state reverts to a sol state to replenish the cytoplasmic supply at the front [25, 26].

Molecular Basis of Sol to Gel Transition

A comprehensive understanding of the molecular organization and regulation of the sol to gel transition remains incomplete. It is currently hypothesized that the sol and gel layers are composed of the same cytoplasmic material, although detailed proteomic profiles of these layers are still lacking. However, in vitro studies have shown that cytoplasmic extracts can transition between gel and liquid states, even demonstrating fluid streaming between the two phases in extracts [27]. Furthermore, reconstituted systems containing actomyosin components have also replicated these properties, suggesting that it is the organizational arrangement of the cytoplasmic components, rather than their composition, that differentiates the sol and gel states [28].

Historically, light microscopy revealed regions of actin enrichment in amoeba; however, the technology at the time was limited in its ability to visualize the organization of actin filaments at the microscale [29]. To observe the microscale organization of filaments many studies turned to scanning electron microscopy (SEM), which enabled detailed visualization of cellular regions known to exist in either sol or gel states. For instance, studies comparing the hyaline cap of the leading edge—characterized by sol state cytoplasm—with the surrounding gel layer revealed striking differences: the sol state cytoplasm contains sparse, thin actin filaments, while the gel layer exhibits both thin and thick filaments arranged into a dense actin network [30, 31]. Intriguingly, these filament structures have also been reconstituted in vitro from cytoplasmic extracts under conditions that induce either relaxation or contraction, thereby mimicking the native sol to gel transitions observed within the cell [32, 33, 34]. While studies utilizing SEM revealed organizational differences between actin filaments in sol and gel states, SEM fails to capture transitions between sol and gel states since it requires fixed samples. The visualization of the active transition between states, as it relates to actin organization, may provide insights as to the regulation of the sol to gel transition and is an active endeavor of the authors. We hope to discuss our insights on the subject matter in subsequent studies.

Efficient Mixing in Laminar Flow

Here we show the amoeba *Chaos carolinensis* uses the sol-gel transition to achieve complete cytoplasmic mixing within a single flow cycle, which we define as the time taken for a particle to traverse the full length of cytoplasmic solution layer and return via the gel layer. This discovery is surprising, given that the cytoplasmic streams in *Chaos carolinensis*, which make up the entire solution layer, exhibits a low Re, and laminar flow. Such conditions typically limit mixing potential, and the gel layer itself imposes even more confinement with even fewer chances for mixing than laminar flows alone would allow.

Our findings indicate that *Chaos carolinensis* overcomes these limitations by inducing sol to gel transitions within the mid-cell region, effectively transferring particles—such as beads and nuclei—between the solution and gel states. This dynamic enables particle exchange across the cytoplasm layers, promoting mixing. We explore this mechanism here by simulating cytoplasmic flow including and excluding mid-cell state switching and comparing mixing behaviors. We validate our simulation by examining the mixing of two bead populations at different time delay intervals, using a method we developed to digitally label each bead population based on tracking data from a single experimental label. Ultimately, we demonstrate that this single-cycle mixing is a result of the amoeba's ability to leverage sol to gel transitions as a powerful natural mixing strategy. These insights not only broaden our understanding of amoeboid cytoplasmic dynamics but also suggest that sol to gel transitions may represent a generalizable mechanism for efficient intracellular mixing in cells with cytoplasmic streaming.

METHODS

Microinjection

Microinjection was used to deliver 20 μm and 10 μm YG fluorescent beads (Polysciences Fluoresbrite® YG Microspheres 20.0 μm, Catalog Number 19096-2, and Polysciences Fluoresbrite® YG Carboxylate Microspheres 10.0 μm, Catalog Number 18142), as well as Histone H1 protein labeled with Alexa-488 (Invitrogen™ Histone H1 From Calf Thymus, Alexa Fluor™ 488 Conjugate, catalog number H13188). All microinjections were carried out using a Drummond Nanoject II system (discontinued), following our own adapted protocol for Drosophila microinjection [35]. A Zeiss Stemi 508 stereo microscope equipped with a Transillumination 300 system and dark field illumination was utilized to visualize the microinjection needle tips easily.

To inject two 20 μm beads into amoeba, the microinjection needle was carefully cut open using a razor under a microscope until the beads could be front-filled. Once the beads were inside the needle, they were positioned near the amoeba and front-filled with low pressure to prevent them from moving too far up the needle. If the beads traveled too high, gravity was used to guide them back down to the tip. Right before the beads were ready to fall out, the needle was swiftly inserted into the amoeba, and a minimal amount of pressure was applied to ensure precise deposition of the two beads into the amoeba's cytoplasmic stream. The same method was employed for injecting 10 μm beads, where 18 beads were loaded and allowed to flow down the tip via gravity before being quickly injected into the amoeba to avoid premature loss of the beads.

This gravity-assisted microinjection technique was essential for the amoeba's survival, as the large diameter of the needle needed for handling 20 μm beads carried the risk of over-injecting, which could cause the amoeba to rupture. However, using this technique, our microinjected cells closely resemble those in control amoebas injected with fluorescent dextran, which is introduced through a standard needle with an opening under 1 μm.

To further ensure amoeba health, we incubate the injected cells for one hour to allow complete wound healing, even though initial wound closure at the injection site appears to occur

within seconds. Importantly, we do not anticipate any adverse effects from the size of our beads to impact the amoeba's health. While controls for un-injected cells are not included here, our routine experiments inserting 100 μm silicon microchips into amoebas—with control studies—demonstrate no adverse effects on amoeba health (data not shown). In these experiments, we assess cell health through crawling speed and pseudopod formation, comparing the injected cells to un-injected cells.

To label nuclei we use Histone H1-Alexa 488, which was commercially available and pre-labeled. To prepare our injectant we resuspended 100 mg of lyophilized histone H1-Alexa 488 in pasteurized spring water. Sodium azide, a toxic preservative, was removed by rinsing the protein with pasteurized spring water three times using 10 kDa spin columns. For microinjection, needles were back-filled with a 5 mg/ml concentration of Histone H1-Alexa 488. To prevent clogging, continuous pressure was applied once the needle tip was broken, and multiple amoebae were injected to maximize the success rate of the injections.

Microscopy

All micromanipulation was done using a Zies Stemi 508 with a Transillumination 300 base. This configuration is equipped with darkfield illumination which is useful for viewing microcapillary needles during micromanipulation. Injected cells were prescreened for fluorescence using a Zeis Axio Zoom V16 before mounting and imaging using other modalities. All samples microinjected with 20 μm beads, 10 μm beads, and Histone H1-488 were imaged using a Nikon Ti2 Inverted Fluorescence Microscope equipped with a Nikon Plan Apo Lambda 4x Objective, a Hamamatsu Ocra-Flash4.0 CMOS camera, and a quad band pass filter. We aimed to have an acquisition frame rate of 2fps while imaging in bright field and the 488 nm fluorescence channel. To achieve this frame rate, we modified our brightfield channel to fire without moving any filters from the fluorescence channel out of the way., The sample in supplementary **figure 3**, along with the sample in supplementary **figure 7,** were imaged using an Olympus FV3000 Confocal microscope using a 60x glycerol objective.

Image Processing

OttoReg pipeline

The OttoReg pipeline was developed for the automated segmentation, cropping, and registration of time-lapse videos of amoeba crawling in a 3 mm diameter well, created using a 120 µm spacer between a coverslip and a glass slide. This pipeline is useful for separating general cellular motion from the motion of intracellular particles to analyze the motion of particles with Mean Squared Displacement (MSD) (**Fig. 1**). The OttoReg pipeline consists of three separate modules, all written in MATLAB. The first module, OttoSeg, uses a maximum intensity projection to generate a background image, which is then subtracted from every frame of the video to produce segmented frames. Variations of this approach include using a median intensity projection to compensate for fluctuations in transmitted light sources, and a rolling projection to generate a series of background images over time. The rolling projection is especially useful for cases where bubbles form inside the spacer during long time-lapse acquisitions, helping to maintain accurate segmentation. The second module, OttoCrop, takes the segmented frames from OttoSeg and binarizes each one to generate a centroid, which is then used for automated cropping. The user defines the crop height and width, which are applied uniformly to all frames. The final module, OttoReg, performs image registration across time for all cropped frames using an image registration configuration created with MATLAB's Image Registration Estimator tool.

All modules have been optimized for speed to handle the 10 TB of data generated from image acquisitions. To achieve this, the pipeline is designed to support multicore processing using MATLAB's Parallel Computing Toolbox.

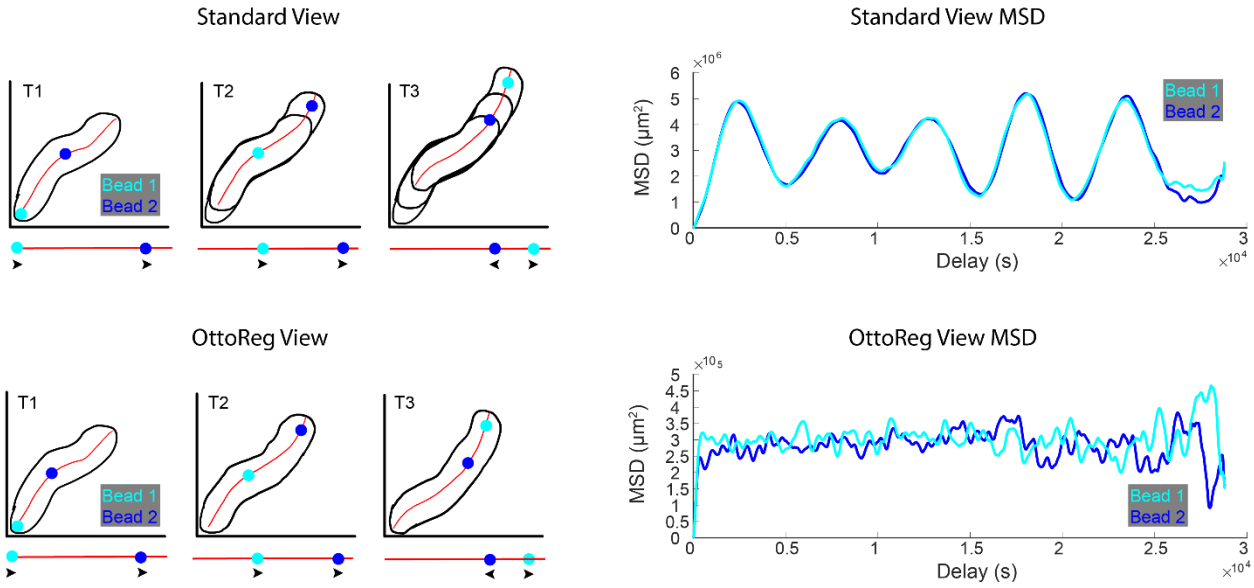

Fig. 1 Separating Bead Movement From Cell Movement Using OttoReg

Figure 1. Separating Bead Movement from Cell Movement Using OttoReg
This figure demonstrates the effect of the OttoReg pipeline on separating bead movement from cell movement during tracking. The left panels (T1, T2, T3) show the trajectories of two tracked beads (cyan for Bead 1 and blue for Bead 2) over time in both the Standard View (top row) and the OttoReg View (bottom row). In the Standard View, both bead movement and overall cell movement are conflated, as shown by the shifting cell outline and bead positions. The OttoReg View corrects for cell movement, isolating the true motion of the beads within the cell. The right panels show the mean squared displacement (MSD) plots for both beads in the Standard View and OttoReg View. In the Standard View MSD, oscillations are evident, likely due to cell movement, while in the OttoReg View, these oscillations are reduced, providing a clearer representation of the actual bead motion independent of the cell's overall movement.

Computational Analysis

Geodesic distance

Our analysis of mixing dynamics is based in part on pairwise distances between beads, in which the temporal dynamics with which such distance increases can be used to classify the type of fluid motion. Using geodesic distance to measure distances within our amoeba's cytoplasm is essential for accurately capturing spatial relationships as the cell is not convex, and constantly changes shape and extends multiple pseudopods. Unlike Euclidean distance, which measures a straight-line path, geodesic distance follows the actual curved route along the amoeba's body, reflecting the shortest path through its complex and shifting landscape. This distinction is illustrated in **figure 2**, where the Euclidean distance between two points in the amoeba (left

panels) differs significantly from the geodesic distance (right panels). The Euclidean measure, shown as a direct line, fails to account for the amoeba's contours and structural boundaries. In contrast, the geodesic distance follows the organism's curved shape, adapting as the amoeba changes form. This approach provides a more realistic and meaningful measurement of separation within the dynamic environment of the amoeba, accommodating its irregular morphology and continuous structural changes. While more accurate, we note that the geodesic distance calculation takes significantly longer than the Euclidean distance calculation. This is because the distance between the bead and every possible pixel has to be calculated for each frame.

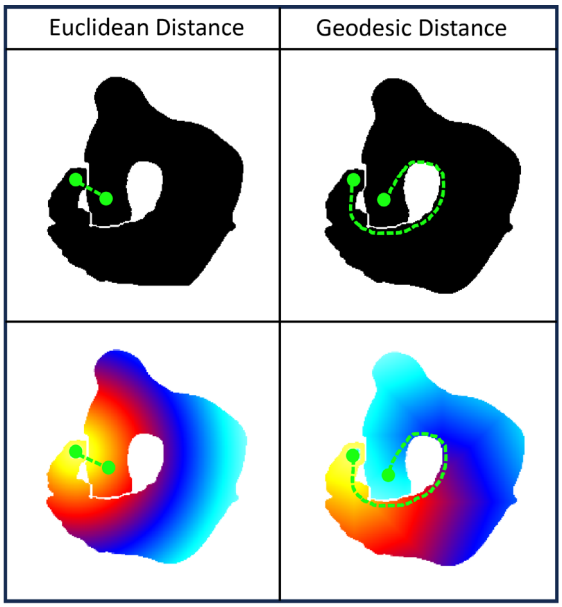

Fig. 2 Euclidean Distance vs. Geodesic Distance

Figure 2. Euclidean Distance vs. Geodesic Distance
This figure compares the differences between Euclidean distance and geodesic distance within a binary image of an amoeba. The left column illustrates the Euclidean distance, where the shortest path is calculated in a straight line between two points, even if obstacles are present. The right column shows the geodesic distance, which accounts for the object's geometry and calculates the shortest path along the surface. The top row displays the binary representation of the two-distance metrics, while the bottom row shows the corresponding distance gradients with color-coded heat maps, where warmer colors represent shorter distances, and cooler colors represent longer distances. The geodesic distance, as shown, correctly follows the contour of the shape, while the Euclidean distance disregards the object's boundaries.

Continuous bead tracking

Bead tracking was performed using the TrackMate plugin in ImageJ [36], with subsequent analysis carried out in MATLAB by loading the spot and track data into spreadsheets. Tracking multiple particles presents a significant challenge, especially when more than two beads are microinjected into a cell, as it complicates continuous trackability. For example, tracking two beads can produce two trajectories that span the entire video. However, when tracking multiple beads, accuracy decreases, often causing tracks to break mid-trajectory. This results in multiple tracks being generated for a single bead.

In our dataset, which contained 18 microinjected 10 μm beads, we generated a total of 54 tracks. To analyze this video effectively, we developed a MATLAB script that identifies overlapping tracks. This allowed us to isolate video segments containing 18 continuous tracks that span the entire length of the video segment. Using this method, we were able to digitally label two distinct bead populations based on their known trajectories, enabling us to study how quickly these two labeled populations mixed over time.

This algorithm allowed us to observe multiple mixing events within a single video and gave us the flexibility to analyze mixing starting at any chosen frame. We leveraged this to examine mixing across different delay times.

Parameters for simulation

To study mixing from two bead trajectories, we track them over time and extract key parameters such as the diffusion coefficient, mean velocity, and dwell time for the respective gel and liquid states. To classify these states, we first apply a 20-second rolling mean squared displacement (MSD) across each bead's trajectory, generating an array where each frame corresponds to the MSD across time within the 20 second window. We then apply a threshold against the 20 second window MSD to distinguish gel states from liquid states. The accuracy of this threshold is verified post-analysis by generating a video overlay that highlights the gel and solution/liquid state trajectories.

Once the gel and liquid segments are identified for each trajectory, MSD analysis is applied to these track subsets to derive diffusion coefficients and mean velocities by fitting a diffusion with drift model to the MSD curve for each state. These parameters are then used to simulate bead movement, allowing us to assess mixing based on the simulation results.

Hyper mixing simulation

We used a structured element matrix in MATLAB to model the movement of 2,500 beads, divided into two groups of 1,250. At T0, all beads are evenly distributed over a 200 μm x 200 μm plane at z = 0, representing the liquid layer. This layer is split across the middle of the Y axis to initiate separate groups at T0. As time progresses, this sheet moves in the positive Y direction, with additional layers at z = 20 and z = -20 representing the exterior gel layers of the amoeba. For each bead, its XY position and layer (upper gel, lower gel, or liquid associated) is stored, along with a clock variable that tracks the time until the next state transition between layers. When beads in the liquid layer (z = 0) reach Y = 200 (the front of the cell), they either shift up or down into the gel layers, which flow in the negative Y direction. In addition to switching layers at Y = 200 for beads in the liquid layer, or at Y = 0 for beads in the gel layers, beads can also change layers at any point before reaching the end of their respective layers based on the dwell time in the current state (see below).

The simulation is carried out in three primary sections, each implementing specific rules. The first section, the "stepping section," moves all beads in their respective directions—liquid beads flow in the positive X direction, while gel beads flow in the negative X direction as the gel treadmills backwards in the reference frame of the cell. Here movement in the Y direction is driven through diffusion to reflect the properties of laminar flow. We used a Gaussian model based on Einstein's formula for diffusion to simulate these steps [37,38]. The step size for each bead is determined using a random number drawn from a Gaussian distribution, fitted to the experimentally derived diffusion coefficient and mean velocity ranges.

In the second section, we check for beads that have moved past the XY boundaries of their respective layers. Beads reaching the end of their layer will switch states, moving from liquid to gel or vice versa. In our simulations, the probability of switching to either gel layer is set to 50% since we don't have experimental data to fit a distribution to model the gel layer selection.

In the third section, beads that have switched states are assigned a clock state drawn from a dwell time distribution. For all beads, the clock is decremented each time-step, and when the clock reaches zero, the bead switches states regardless of whether they have reached the end of their current layer. Once this happens a new value is updated, and the clock is reset. The first clock value is assigned for every bead at T0. Clock values are generated using a random number, fitted to a distribution based on experimental dwell time data for gel and liquid layers. The most appropriate distribution is selected by testing several models and choosing the one with the lowest AIC value.

To assess the impact of layer switching caused by the third section of our simulation, we ran the simulation without this feature, referring to it as "standard mixing." When all three sections are enabled, including the layer switching, we refer to it as "hyper mixing."

SMI and SNN metrics

To quantitatively measure mixing across time in our simulation data, we use two distinct mixing metrics. The first, the Subdomain Mixing Index (SMI), evaluates the fraction of different bead populations within fixed subdomains [39]. Subdomain-based methods divide the system into smaller, defined regions or "bins" to quantify the distribution of distinct bead populations within each subdomain. This approaches evaluate mixing by comparing the relative proportions of bead types in each region to an ideal mixed state. In the SMI, each subdomain is weighted based on the number of beads it contains relative to the total population. The sum of these subdomain fractions gives the SMI. Although the SMI was formulated to handle multiple distinct populations within a given space[39], we have simplified the SMI formula to handle two distinct populations. The SMI is calculated as follows:

Formula 1: Subdomain Mixing Index (SMI)

Let:

- $S = 192$ be the total number of subdomains.
- B be the total number of beads.
- n_s be the number of beads in subdomain s, where $s = 1, 2, \ldots, S$.
- f_s be the larger fraction of different bead populations within subdomain s.
- Each subdomain is weighted by the ratio $\frac{n_s}{B}$.

The Subdomain Mixing Index (SMI) can be expressed as:

$$\text{SMI} = \sum_{s=1}^{S} \frac{n_s}{B} f_s$$

where:

- $\frac{n_s}{B}$ is the weight of subdomain s, representing its proportion relative to the total population.
- f_s is the smaller fraction of 2 different bead populations within subdomain s.

In other words, the SMI is calculated by summing the weighted fractions of different bead populations across all 192 subdomains.

The SMI metric is particularly useful for measuring mixing in fixed spaces, like those represented in our simulation. The SMI accurately determines the length of time it takes for a system to reach a stable mixing state [39]. While adjusting subdomain size can affect the overall mixing magnitude reported, it has no impact on the time it takes to reach a stable state.

Our second metric, the Simple Nearest Neighbor (SNN) score is designed for dynamic environments, such as inside a shape-changing amoeba. Neighbor-based methods to calculate mixing focus on the immediate surroundings of individual beads, analyzing how the local environment contributes to overall mixing. The SNN metric calculates the fraction of mixing by summing the fractions of similarly labeled beads from the nearest five neighbors for each bead, thereby avoiding the limitations of fixed space. The SNN is calculated as follows:

Formula 2: Simple Nearest Neighbor (SNN)

Let:

- B be the total number of beads.
- For each bead j (where $j = 1, 2, \ldots, B$), we find the five nearest neighbors using Euclidean distance.
- For each of the 5 nearest neighbors of bead j, we create bead pairs and score them as follows:
  - If a bead pair has the same color, it scores 0.
  - If a bead pair has different colors, it scores 1.

The SNN calculation formula can be expressed as:

$$\text{SNN} = \frac{1}{B} \sum_{j=1}^{B} \frac{1}{5} \sum_{k=1}^{5} \delta(C_j, C_{jk})$$

where:

- C_j is the color of bead j.
- C_{jk} is the color of the k-th nearest neighbor of bead j.
- $\delta(C_j, C_{jk})$ is an indicator function that outputs 1 if $C_j \neq C_{jk}$ (different colors) and 0 if $C_j = C_{jk}$ (same color).

In other words, the formula calculates the fraction of mixed pairs (different colors) for each bead based on its five nearest neighbors, and then averages this fraction across all beads to obtain the final SNN metric.

This more flexible approach allows us to measure mixing without the need for subdomains. To test the accuracy of our mixing metric, we plot it against the SMI and show similar results. In addition to using the SNN directly across time in our simulations, we also use the mean SNN across time delays to quantify mixing in experimental data. Time delays provide a comprehensive view of the entire mixing process, making it possible to understand how well two populations mix and whether the mixture remains stable over time. The mean SNN across time delays is calculated as follows:

Formula 3: mean SNN across time delays

Let:

- d be the delay in seconds.
- N be the total number of frames (15000) at 2fps.
- $\mathrm{SNN}(i, d)$ be the SNN calculation for the i-th frame at delay d.

$$\mathrm{Mean}_{SNN} = \frac{1}{N - d * 2} \sum_{i=1}^{N-d*2} \mathrm{SNN}(i, d * 2)$$

Where:

- $(N - d * 2)$ is the number of frames for which the SNN calculation is valid, as the delay reduces the number of pairs available for the calculation.
- Here the delay in time is multiplied by 2 to transform it into a delay in frames since the frame rate interval is 0.5 seconds.

To apply these equations to experimental data, we developed a computational method to designate two distinct bead populations from a single experimentally injected label, allowing us to study mixing across delays. This was achieved by tracking individual beads and computationally assigning each trajectory one of two separate colors based on the minor axis orientation which essentially splits the amoeba down the middle the short way then assigns a color for beads on either side, which is consistent with our scheme for labelling beads in the simulations.

RESULTS

Observations of Sol and Gel Layers

Our first step to understanding mixing is to characterize the fluid flow as a function of position in the cell, since it is this flow that is thought to generate the mixing. The morphology of the amoeba consists of two layers of gel sandwiching a layer of solution that streams through a mechanism involving the selective blebbing of the actin cortex at the leading edge (**Fig 3.1**, **Fig 3.2**). The leading edge maintains a continuous solution to gel state transition. Meanwhile, the rear of the cell, known as the uropod, maintains a continuous gel to solution state transition. While gel and solution states are easily distinguishable within these regions of the cell, we sought to provide evidence for laminar flow in the solution state layer and to determine the thickness of solution and gel state layers at the mid-cell region where the difference between layers is not as obvious. To search for laminar flow and the border between solution and gel state layers we turned to Particle Image Velocimetry (PIV). PIV is an optical measurement technique used to measure fluid flow by tracking the movement of particles within fluid. PIV adopts an Eulerian approach, focusing on fixed points within a flow field and measuring how the fluid moves through these points over time. This contrasts with a Lagrangian approach, which would track individual particles as they move through the flow. By capturing velocity information across a grid of fixed points, PIV provides a comprehensive, instantaneous map of flow patterns rather than following individual particles along their paths. This makes PIV particularly useful for studying complex, spatially distributed flow fields. Using PIV, we traced the bulk flow of cytoplasmic vacuoles, vesicles, and refractile bodies observed in our transmitted light timelapse acquisitions. We detected laminar flow streamlines in cytoplasmic streams (**Fig 3.3**), confirming our assumption that cytoplasmic streams are laminar. We used the sum of velocities, u and v components, to find interfaces between different flows, which effectively marks the borders between sol and gel states in the mid-cell region (**Fig 3.4**). From these measurements we note the gel phase is roughly 40 μm on either side with the solution

phase being 80 – 100 µm. Without PIV analysis the border between solution and gel states would be indistinguishable in this region of the cell (**Fig 3.5**).

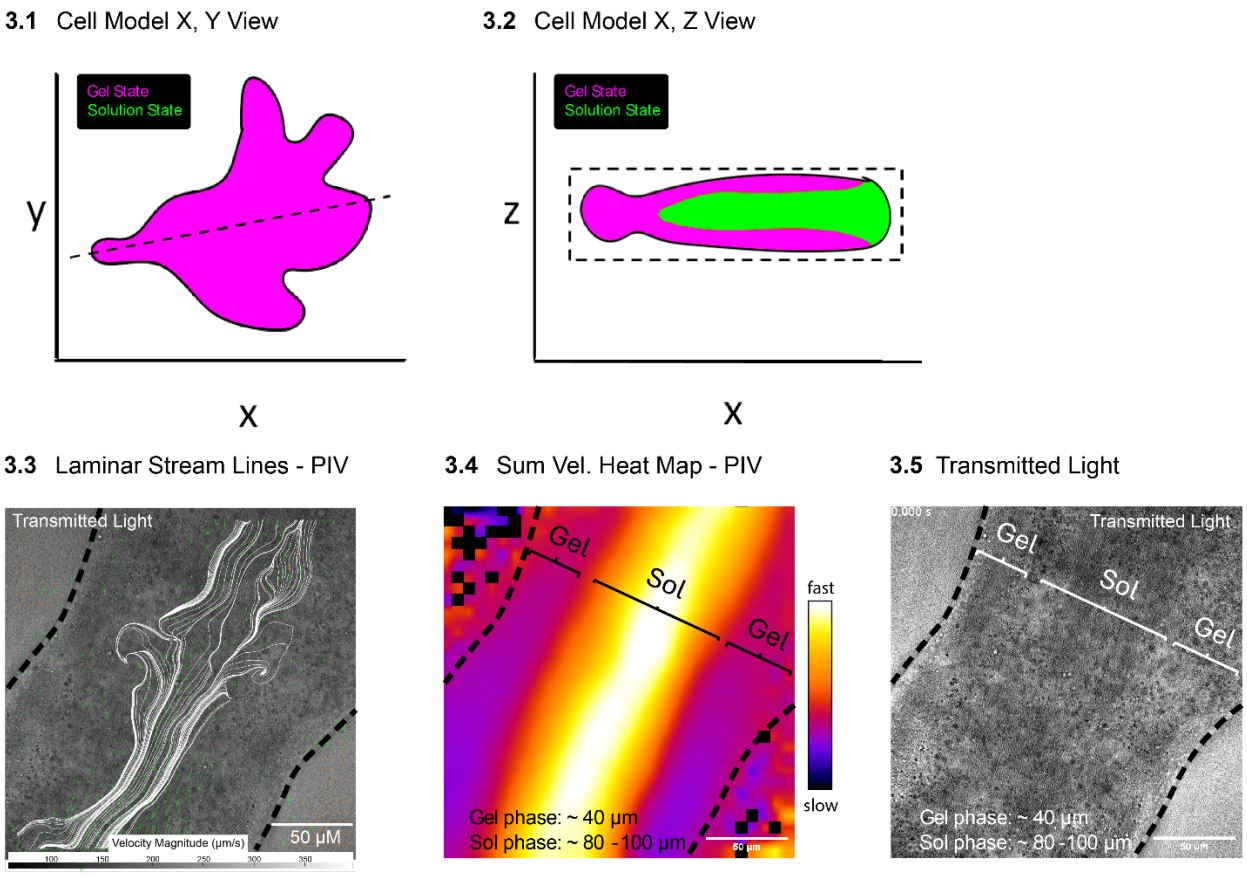

Fig. 3 Solution and Gel State Laminar Flow in Liquid State Cytoplasm

Figure 3. Solution and Gel State Laminar Flow
This figure illustrates the morphological distribution of gel and liquid states within an amoeba. 3.1 Cross-sectional view in the x-y plane highlights the overall shape of the amoeba. 3.2 Side view (x-z-plane) shows the stratification of states along the length of the cell. The dashed line marks the axis of view for the side projection, with the liquid state concentrated in the central core, surrounded by the gel state. The dashed line marks the axis of view for the side projection. This highlights the spatial dynamics of cytoplasmic sol to gel transitions in amoeboid movement. 3.3 Laminar flow streamlines obtained from particle image velocimetry (PIV) analysis in the liquid (sol) state of the cytoplasm. The streamlines illustrate the smooth, parallel flow of cytoplasmic contents in this region. The dashed line indicates cell boundary. The flow velocity is measured in microns per second (µm/s), with a scale bar representing 50 µm. 3.4 Heat map showing the sum of velocity magnitudes in the solution and gel phases of the cytoplasm. The warmer colors represent faster velocities, while cooler colors correspond to slower velocities. Gel and sol regions are marked, showing a clear difference in flow characteristics across these mid-cell regions. 3.5 Transmitted light image showing the distinct separation between gel and sol regions in the amoeba's cytoplasm. The boundaries are labeled accordingly, and the gel phase (~40 µm) and sol phase (~80–100 µm) thicknesses are noted. The dashed lines mark the cell boundary.

Close Bead Pairs Separation Events

Next, we quantified separation of marker beads under the action of cytoplasmic flow. Fitting a power law exponent to describe how the interparticle distance increases over time, for pairs of beads that are initially close together, can quantify how efficiently cells mix. In mixing processes, the distance between particles often grows according to a power law relationship. A higher exponent represents faster and more efficient mixing, whereas a lower exponent suggests less efficient mixing or restricted movement, making power law scaling useful for distinguishing between different mixing regimes.

In idealized laminar flows, such as those observed in cytoplasmic streaming (**Fig. 3.3**), particles move in smooth, ordered layers. These systems typically exhibit lower mixing efficiency compared to turbulent flows because the movement is steady and predictable, leading to regular, non-chaotic particle separation [40]. While laminar flows can sometimes display linear growth in distance similar to ballistic regimes, they inherently lack the high mixing efficiency of turbulent systems. For example, in boundary layers along flat plates under laminar flow conditions, fluid particles near the surface can show linear displacement for short times due to the constant shear. The displacement in this layer follows a nearly linear progression before any significant deviation due to mixing or turbulence. The power law of 1, characteristic of ballistic regimes, reflects steady, linear separation [41,42]. However, laminar flows are more commonly associated with a lower power law exponent. In these cases, the system exists in the sub diffusive regime with power law exponents between 0 and 0.5 [37, 43, 44], indicating very slow mixing [45].

When particles encounter chaotic behavior or eddies within turbulent systems, the power law exponent typically falls between 0.5 and 1, a range known as the super-diffusive regime [46, 47]. This regime represents mixing that occurs more efficiently than in laminar flows, but it does not follow the perfect linearity of ballistic behavior. This transitional turbulence causes the chaotic motion of particles, leading to accelerated mixing. In contrast, ballistic behavior (power law of 1)

represents linear growth and typically occurs when particles move at constant velocity, such as during the early stages of dispersion or when forces act uniformly on the particles [48, 49].

In the super-ballistic regime, where the power law is greater than 1, particles experience faster-than-linear separation. This phenomenon is often associated with shock waves or explosive mixing, where particles are driven apart at an accelerating rate [42, 50]. Such systems exhibit the highest mixing efficiency due to the rapid dispersion of particles.

In our data, power law fits for geodesic interparticle distance (**Fig. 2**) were distributed across different regimes (**Table 3**). The majority were in sub-diffusive regimes (power law between 0 and 0.5) and super-diffusive regimes (power law between 0.5 and 1), with a few outliers in the super-ballistic regime. We measured the interparticle distance for 169 bead pair separation events across 4 different experimental samples and fit a power law exponent to describe the interparticle distance as a function of time for each event, observing similar results for all four samples (**Fig.4**, **Sup. Fig. S1** – **Sup. Fig. S3**). Our results indicate that 7% of the total separation events (12 events) were super-ballistic, with a power law exponent slightly greater than 1. 39% of the events (66 events) were super-diffusive (exponent between 0.5 and 1), and 46% (78 events) were sub-diffusive (exponent between 0 and 0.5). Lastly, 3% of the events (4 events) exhibited a power law exponent slightly below 0, indicating that the beads moved closer together by the end of the assay due to trajectories crashing into the cell boundary.

Most bead separation events fell within the super-diffusive regime, with only a few entering the super-ballistic regime. However, we observed no turbulent flows or explosive events to account for these findings. To better understand these anomalies, we conducted a mean squared displacement analysis (MSD), which helps identify sub-diffusive, diffusive, and super-diffusive segments of time in individual trajectories. Upon analyzing the MSD of the super-diffusive and super-ballistic separation events, we found that 67% (52/78) of these events featured one bead with a super-diffusive trajectory while the other had a sub-diffusive or restricted trajectory. This

pattern suggests that one bead was flowing in the liquid state while the other was trapped in the gel state. In contrast, 33% (26/78) of the super-diffusive and super-ballistic separation events had both beads following super-diffusive trajectories, indicating that both beads were flowing with the liquid state flow, possibly into different pseudopods.

Table 3. Summary of Regimes Based on r(t) ∝ t^{α}
This table categorizes different regimes of particle separation based on the power-law exponent α, which describes how the distance between particles scales with time. The regimes range from super-ballistic (rapid, faster-than-linear separation) to localized or stagnant, where no separation occurs. Each regime's associated separation growth, mixing efficiency, and typical example scenarios are listed as examples for how mixing behavior changes across different systems.

Table 3: Summary of Regimes Based on $r(t) \propto t^{\alpha}$

Power-law Exponent α	**Regime**	**Separation Growth**	**Mixing Efficiency**	**Example Scenario**
$\alpha > 1$	Super-ballistic	Faster than linear	Very high	Shock waves, explosive mixing
$\alpha = 1$	Ballistic	Linear	High	Early stages of turbulent dispersion
$0.5 < \alpha < 1$	Super-diffusive (Turbulent)	Slower than linear but faster than diffusion	High	Richardson law in turbulent flows
$\alpha = 0.5$	Diffusive (Brownian)	$t^{0.5}$ (sub-linear)	Moderate	Molecular diffusion, Brownian motion
$\alpha < 0.5$	Sub-diffusive	Very slow separation	Low	Diffusion in constrained systems, porous media
$\alpha = 0$	Localized/Stagnant	No separation	None	Static systems, trapped particles

4.1 20µm Yellow Green (YG) Fluorescent Bead Microinjection in Amoeba Chaos n1

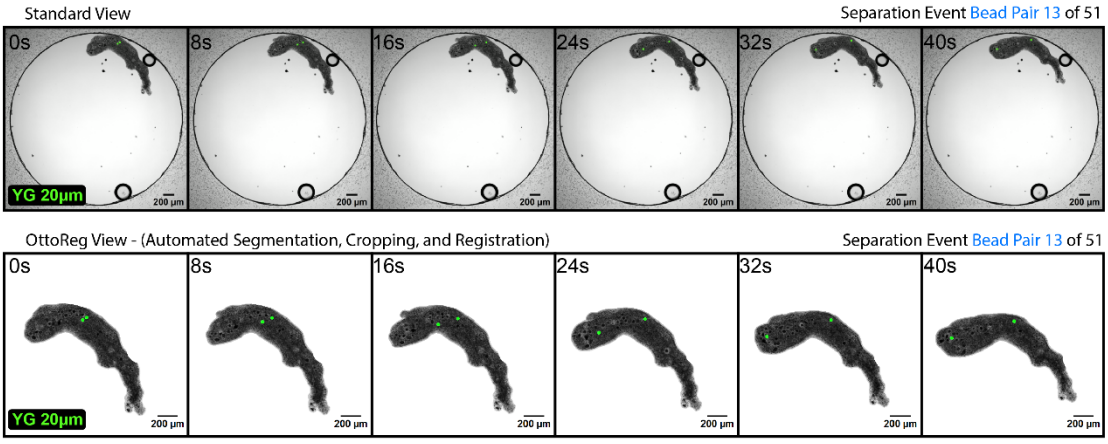

4.2 Inter Partical Distance Over Time n1

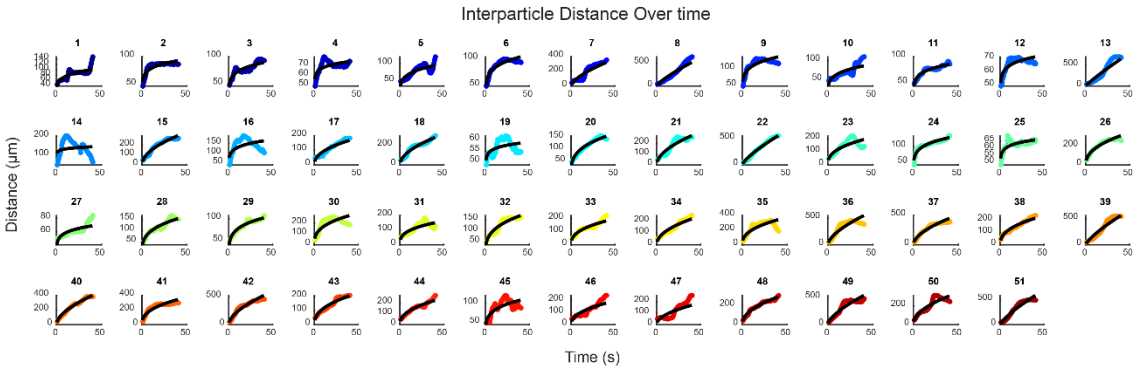

4.3 Power Law Exponent for Time with Respect to Interparticle Distance n1

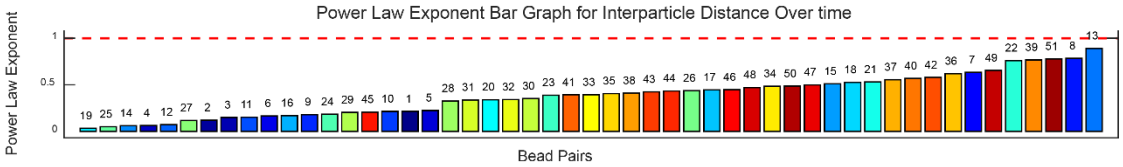

4.4 Mean Squared Displacement for Bead Pair Trajectories n1

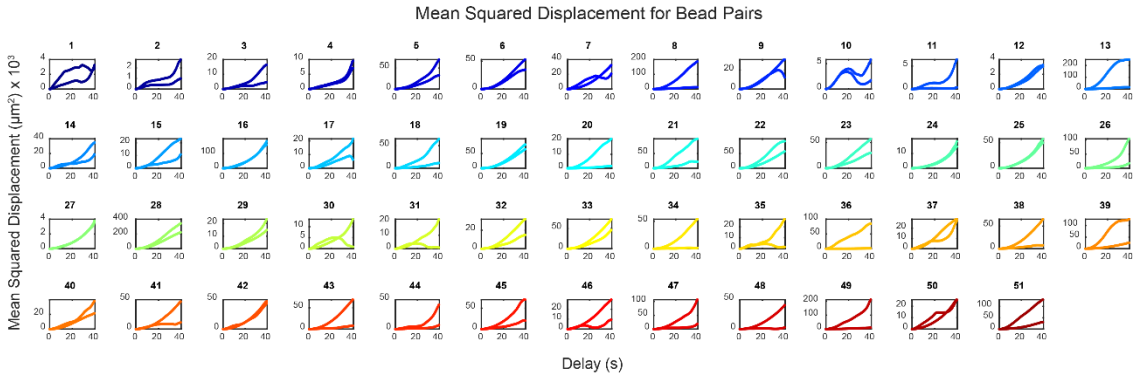

Fig. 4 20µm Bead Separation Assay n1 of 4

Figure 4. 20 µm Bead Separation Assay n1 of 4
4.1 Time-lapse images showing the microinjection of 20 µm yellow-green (YG) fluorescent beads into Amoeba *Chaos*. The top row presents the standard view, and the bottom row shows the OttoReg view, where automated segmentation, cropping, and registration have been applied. The images capture a separation event for bead pair 13. Scale bars represent 200 µm. 4.2 Interparticle distance over time for each bead pair tracked throughout the experiment. Each plot corresponds to a bead pair, displaying the distance (µm) between beads over time (s). 4.3 Power law exponent for interparticle distance as a function of time. The bar graph shows the power law exponent for each bead pair, with values color-coded and labeled. The red dashed line is placed at Y = 1. 4.4 (MSD) plots for each bead pair trajectory. These plots show the MSD (µm²) as a function of delay time (seconds), providing insight into the diffusion behavior of the beads within the amoeba.

Pseudopod Modulation and Separation Rate

We speculated that pseudopod formation, migration, and resorption might drive mixing similar to the Baker's Transformation in which a region of space is deformed and then folded over. It is named the Baker's Transformation because its action resembles the traditional folding and stretching of dough by a baker. The transformation is particularly useful in understanding how repeated stretching and folding operations lead to efficient mixing in confined spaces, and it is a classic example in the field of chaotic dynamics [52, 53]. In theory, complete mixing requires infinitely many cycles, but in practice, near-complete mixing can often be achieved after just 5 to 10 cycles using the Baker's Transformation [52, 53]. In this view, the differences in motion between bead pairs in our previous section might correspond to entry of one bead into a pseudopod followed by motion of the pseudopod in a new direction. In such a situation, pseudopods would be playing a central role in determining bead motion, such that.an increase in pseudopod number should lead to a higher frequency of ballistic and super diffusive bead pair separation, and reduction in pseudopod number leads to reduced bead separation.

To test this idea, we used non-chemical perturbations to modulate pseudopod number in microinjected bead pair time-lapse experiments. We compared the power law exponents across three experimental groups: methyl cellulose at 25ºC, to increase pseudopod number; water at 37ºC, to decrease pseudopod number; and water at 25ºC as the control, reused from the previous section (**Fig 5.1**). To assess the effectiveness of our treatments in modulating pseudopod number,

5.1 Non-chemical Pseudopod Modulating Conditions

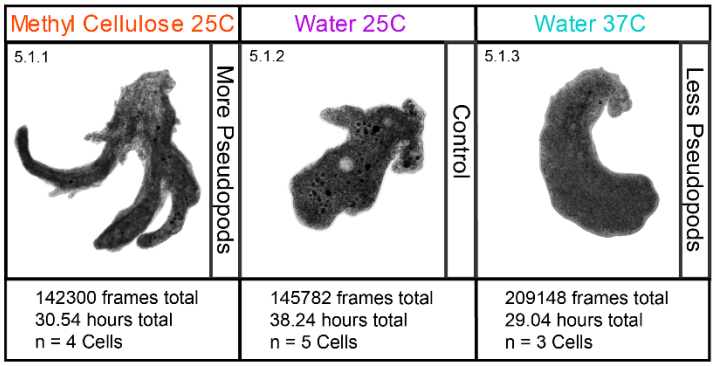

5.2 Pseudopod # Readout

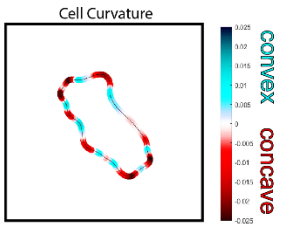

5.3 Concave Sum Comparison

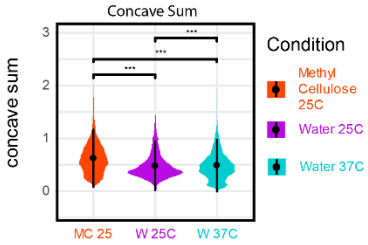

5.4 Bead Pair Separation Events

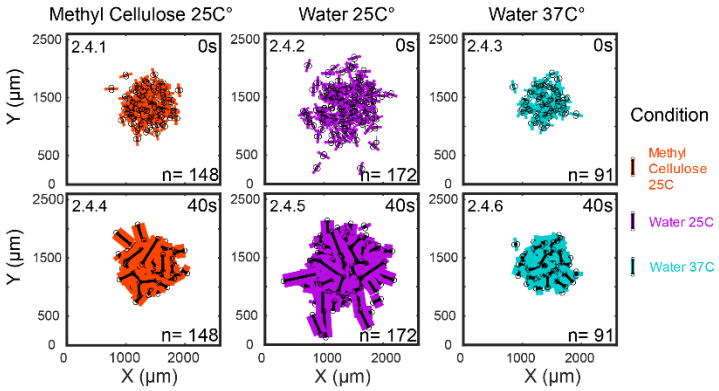

5.5 Power Law Exponents

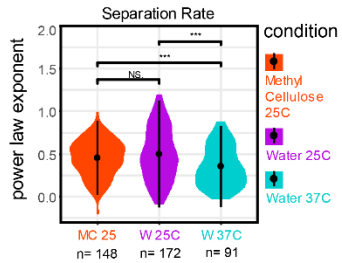

Fig. 5 Bead Separation Rate and Pseudopod Number

we monitored concave cell curvature in all frames for every time-lapse acquisition (**Fig. 5.2**). Our analysis showed a significant difference in the concave sum across frames (**Fig. 5.3**), confirming the effectiveness of our pseudopod modulating conditions. We also plotted the start and end of each bead pair separation event for every group (**Fig. 5.4**). Despite seeing a significant increase in pseudopod number in the methyl cellulose at 25ºC group compared to the water at 25ºC control, we found no significant difference in the power law exponents between the groups (**Fig. 5.5**), suggesting that an increase in pseudopods may have minimal or no effect on the overall mixing outcome.

Figure 5. Bead Separation Rate and Pseudopod Number
5.1 Non-chemical pseudopod modulating conditions: 5.1.1–5.1.3 Time-lapse images showing amoeba in three different environmental conditions: Methyl Cellulose at 25°C, Water at 25°C, and Water at 37°C. The methyl cellulose condition at 25°C increases pseudopod number whereas the water condition at 37°C reduces pseudopod number. The water condition at 25°C represents normal number of pseudopods. The total number of frames, hours recorded, and number of cells (n) are indicated. 5.2 Pseudopod number readout: Cell curvature analysis is shown, where convex (blue) and concave (red) regions along the cell outline correspond to areas where pseudopods are found. 5.3 Concave sum comparison: Violin plot showing the distribution of concave sums under different environmental conditions (Methyl Cellulose 25°C, Water 25°C, and Water 37°C). The asterisks indicate statistically significant differences between conditions, marking the effectiveness of pseudopod modulation under these conditions. 5.4 Bead pair separation events: Scatter plots showing the position of bead pairs under the three conditions at time 0 seconds (top row) and 40 seconds (bottom row). The number of bead pairs (n) for each condition is indicated. 5.5 Power law exponents: Violin plot showing the separation rate (power law exponent) for bead pairs across the three environmental conditions. Significant differences between conditions are indicated by asterisks, with "NS" indicating non-significant differences.

Gel and Liquid State Observations

To further investigate the flow dynamics within the solution and gel state layers, we measured the dwell time distribution, diffusion coefficients, and mean velocity of 20 μm beads moving through each state. Since each bead trajectory includes multiple transitions between solution and gel layers, we segmented and classified the flow states within individual trajectories to analyze the properties of each layer separately. To classify states, we first applied a rolling mean square displacement (MSD) and assigned an MSD value to each time point (**Fig 6.1 - Fig 6.3**). Using an MSD threshold, we then distinguished between solution and gel states, generating dwell time segments for each state along individual trajectories (**Fig 6.4**).

The MSD threshold was fine-tuned by overlaying videos of bead movement with color-coded bead states—green for liquid state flow and magenta for gel state flow. By testing various threshold values, we identified the most accurate labeling threshold. This approach was feasible for quality control because bead state transitions are visually clear, as the direction of flow reverses when beads switch states (**Fig 6.6**).

After classifying states, we fit mean MSD curves to the segments corresponding to solution and gel states, calculating diffusion coefficients of 19.6 μm²/s for the gel state and 212 μm²/s for the solution state (**Fig 6.5**). To disentangle the contributions of diffusion and advection in our observed diffusion coefficients (derived from MSD curves), we used the Stokes-Einstein equation. This equation provides an idealized calculation of the diffusion coefficient based on particle size, temperature, and fluid viscosity, assuming pure Brownian motion without any advective influence. It serves as a baseline, allowing us to estimate the expected diffusion coefficient under purely diffusive conditions. The diffusion coefficient is calculated using the following equation given by:

Estimateing diffusion coefficient D with the Stokes-Einstein equation:

$$D = \frac{k_B T}{6\pi\eta r}$$

where:

- $k_B = 1.38 \times 10^{-23}\,\mathrm{J/K}$ is Boltzmann's constant,
- $T = 310\,\mathrm{K}$ is the temperature,
- $\eta = 210\,\mathrm{mPa \cdot s} = 210 \times 10^{-3}\,\mathrm{Pa \cdot s}$ is the viscosity of the cytoplasm,
- $r = 10 \times 10^{-6}\,\mathrm{m}$ is the radius of the bead (for a 20 μm diameter).

Substituting these values, we get:

$$D = \frac{1.38 \times 10^{-23} \times 310}{6 \times 3.14159 \times 210 \times 10^{-3} \times 10 \times 10^{-6}}$$

Calculating this yields:

$$D \approx 1.08 \times 10^{-16}\,\mathrm{m^2/s} = 0.108\,\mu\mathrm{m^2/s}$$

Although no direct viscosity measurements are available for Chaos carolinensis, traction force microscopy has been used to estimate cytoplasmic viscosity in macrophages, which exhibit similar amoeboid movement and cytoplasmic streaming. The cytoplasmic viscosity measured in macrophages is approximately 210 mPa·s, providing a reasonable basis for estimating the role of advection in bead flow within our system. However, it remains unclear whether the reported viscosity in macrophages corresponds to the solution or gel layer. For reference, the estimated

diffusion coefficient for a 20 μm bead in macrophage cytoplasm is approximately 0.108 μm²/s. In comparison, our measured diffusion coefficients for Chaos cytoplasm are significantly higher: 19.6 μm²/s in the gel state and 212 μm²/s in the solution state. This suggests that advection plays a prominent role in Chaos cytoplasmic dynamics.

Additionally, we measured mean bead velocities of 3.44 μm/s in the gel state and 12.8 μm/s in the solution state. Using these values, we calculated the Péclet number (Pe) for each layer. For a bead moving at 12.8 μm/s through the solution layer over a characteristic distance of 1200 μm, with a diffusion coefficient of 212 μm²/s, the Pe is approximately 72.45, which falls within the regime where weak advection is the dominant transport mechanism (**Table 2**). This Pe value aligns with the discrepancy between our observed diffusion coefficients and those estimated via the Stokes-Einstein equation. In contrast, for a bead moving through the gel layer at 3.44 μm/s over the same distance, with a diffusion coefficient of 19.6 μm²/s, the Pe is approximately 210.61 in the gel layer. This value indicates a regime where advection becomes the dominant transport mechanism, with diffusion beginning to play a minimal role, underscoring the confined nature of the gel layer. We note that advection in the gel layer may be explained by the known treadmilling of the actin cytoskeleton. This may be especially pronounced in cells with a uropod, since the uropod consumes the gel layer, driving its retrograde flow. Together, these findings suggest that advection is the primary driver of bead transport within Chaos cytoplasm.

Our dwell time histogram (**Fig 6.5**) shows that most dwell time events last around 20 seconds, with many events also falling under 10 seconds. These short dwell times imply that beads frequently switch between layers before reaching the leading or trailing edges. It is unlikely that diffusion in the z-direction explains this solution to gel state movement. To determine the average time that a bead would take to diffuse out of a 100 μm solution state layer we use the electrostatic approximation given by:

$$\frac{b^2}{12D}$$

where:

- b is the characteristic length or correlation length in the system.
- D is the diffusion coefficient of a particle or molecule in the medium.

The electrostatic approximation estimates it would take 3.93 seconds for a bead randomly placed in the solution layer to diffuse to the gel layer, indicating that mere arrival in the gel layer is insufficient for beads to switch states. This also suggests that biological regulation may play a role controlling the sol to gel transition aside from the physical properties of the cytoplasm.

Our time-lapse videos qualitatively show that beads transition between solution and gel layers before flowing to either the trailing or leading edge, suggesting that the sol to gel transition occurs not only at the cell ends (as traditionally studied) but also in the mid-cell region. Of the separation events in super-diffusive and ballistic regimes, 67% (52 out of 78) featured an MSD profile where one bead followed a super-diffusive trajectory while the other had a sub-diffusive or restricted trajectory (**Fig 4.4**). This dual MSD profile can be explained by three possible scenarios: (1) the beads are simply flowing past each other in separate layers; or (2) and (3) the beads start in the same layer (gel or liquid), but one switches to the other layer. The short dwell time counts (**Fig 6.5**) and observed mid cell state transitions suggest that the solution to gel transition is a dynamic process that occurs everywhere in the cell.

6.1 20 µm Yellow Green (YG) Bead Micoinjection

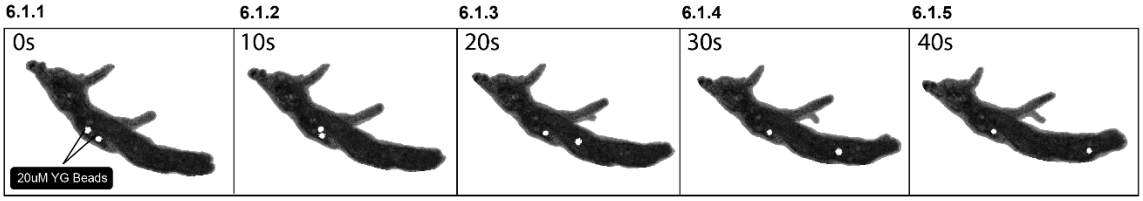

6.2 Rolling 20s Tracks and MSD Curves

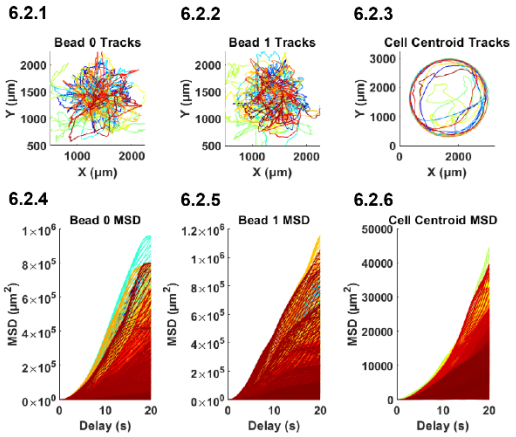

6.3 Mean MSD Across Time

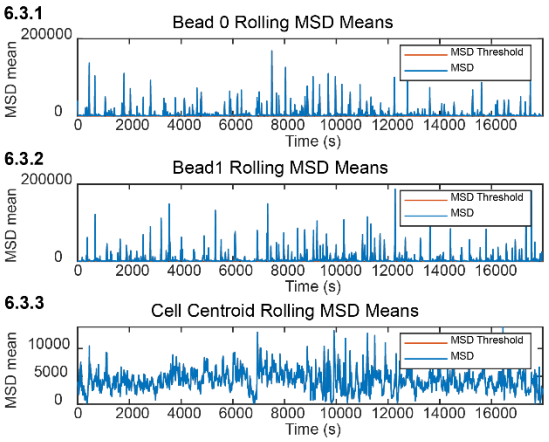

6.4 Gel / Liquid State Detection Using Mean MSD Thresholding

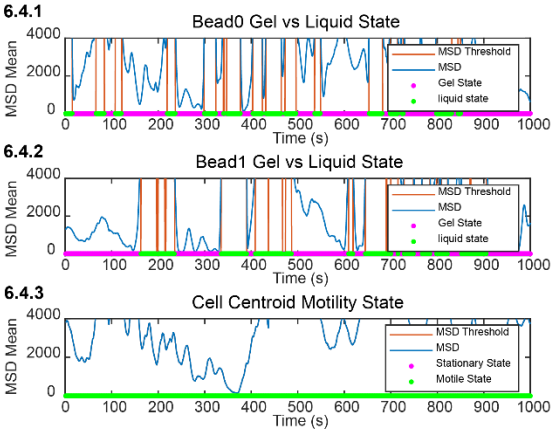

6.5 Gel / Liquid State Dwell Times, Diffusion Coefficients, and Mean Velocity

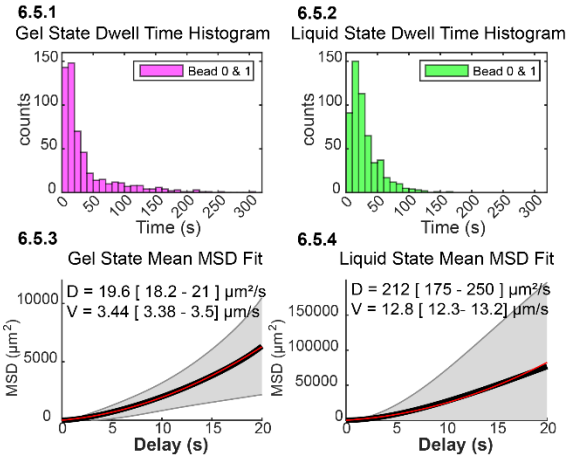

6.6 Gel and Liquid State Flow Labled in 20 µm (YG) Bead Micoinjection Time Lapse

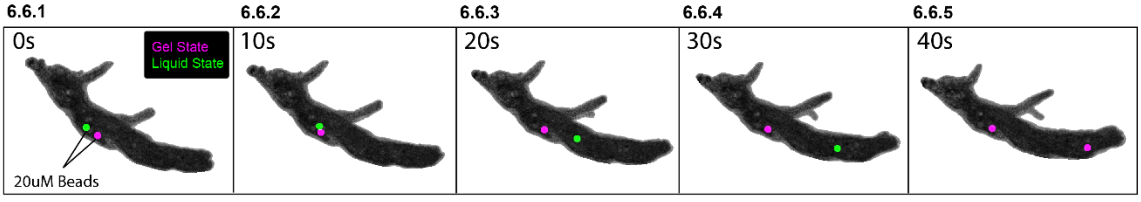

Fig. 6 Extracting Gel and Liquid State Parameters for Mixing Simulation

Figure 6. Extracting Gel and Liquid State Parameters for Mixing Simulation
6.1 Time-lapse images of 20 μm Yellow Green (YG) fluorescent bead microinjection into an amoeba. Bead movement is tracked over time, with images captured every 0.5 seconds from 0 to 40 seconds. 10 second intervals between frames are shown in this panel. 6.2 Rolling 20s tracks and mean squared displacement (MSD) curves - beads and cell centroid. 6.2.1 Bead 0 tracks, showing the trajectory over time. 6.2.2 Bead 1 tracks, showing the trajectory over time. 6.2.3 Cell centroid tracks, indicating the motion of the overall cell body. 6.2.4–6.2.6 Rolling MSD plots for Bead 0, Bead 1, and the cell centroid over time. 6.3 Mean MSD across time from rolling 20s tracks. Rolling MSD mean plotted for Bead 0, Bead 1, and cell centroid (3.3.1–3.3.3). 6.4 Mean MSD across time, with rolling MSD means plotted for Bead 0, Bead 1, and the cell centroid. A Gel and liquid state detection is applied with gel states highlighted in magenta and liquid states highlighted in green (3.4.1–3.4.3). 6.5 Gel and liquid state dwell times, diffusion coefficients, and mean velocity: 6.5.1–6.5.2 Histograms of dwell times for the gel and liquid states for Beads 0 and 1. 6.5.3–6.5.4 MSD fits for gel / liquid states. diffusion coefficients (D) and mean velocities (V). 6.6 Visualization of gel and liquid state flow labeled with 20 μm YG fluorescent beads over time in the microinjection time-lapse.

To observe the viscoelastic properties of the gel layer we immobilized a cell with a minimal concentration of 1 μM [latrunculin B] and observed the motion of an undigested rotifer in its gel layer. While the minimal latrunculin B treatment immobilized our amoeba, it had little to no effect on the rotifer's movement (**Fig 7.1**). Using PIV on transmitted light microscopy timelapse data, we examine the effect of the confined rotifer's movement across the gel layer. When the rotifer moves, the PIV data shows velocity magnitude extending over a long distance across the gel layer (**Fig 7.2**). The flow propagating well beyond the rotifer itself suggests that the gel layer is elastic enough to transmit movement across a broad area rather than dissipating it locally, which is characteristic of viscoelastic or elastic materials. This elasticity likely supports the amoeba's shape maintenance and structural integrity, even as it undergoes dynamic changes during movement and pseudopod formation.

7.1 Time Lapse of Rotifer Inside of Amoeba Treated with 1µM [LatB]

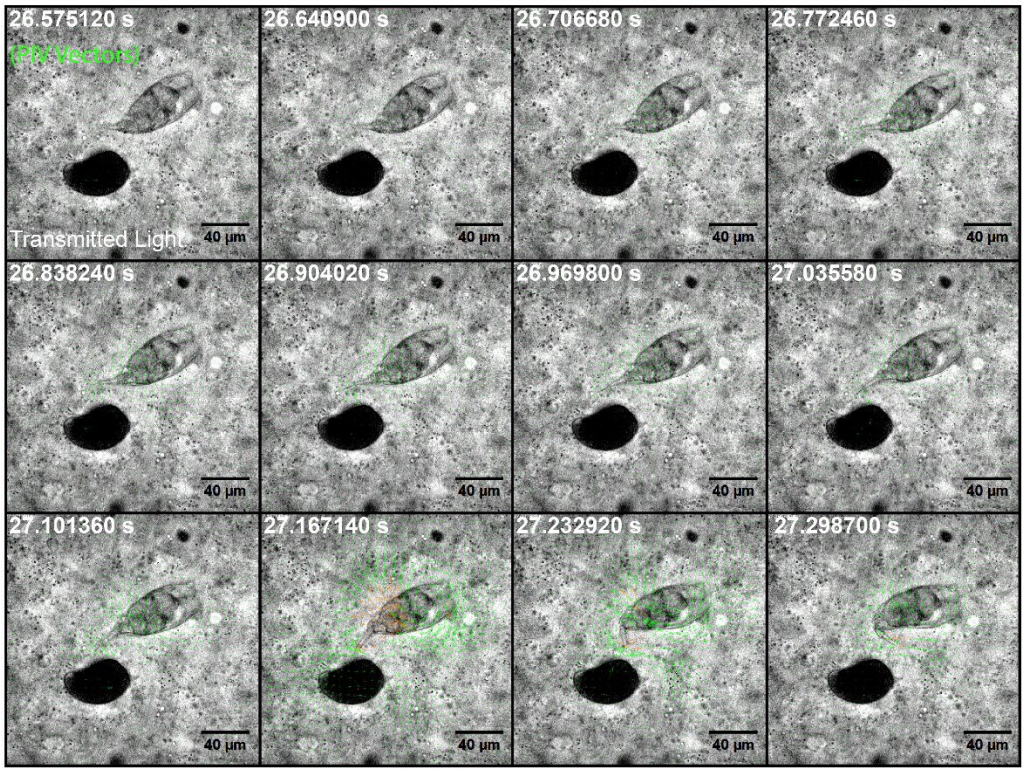

7.2 PIV Vector Overlay on Heat Map of Vector Magnitude

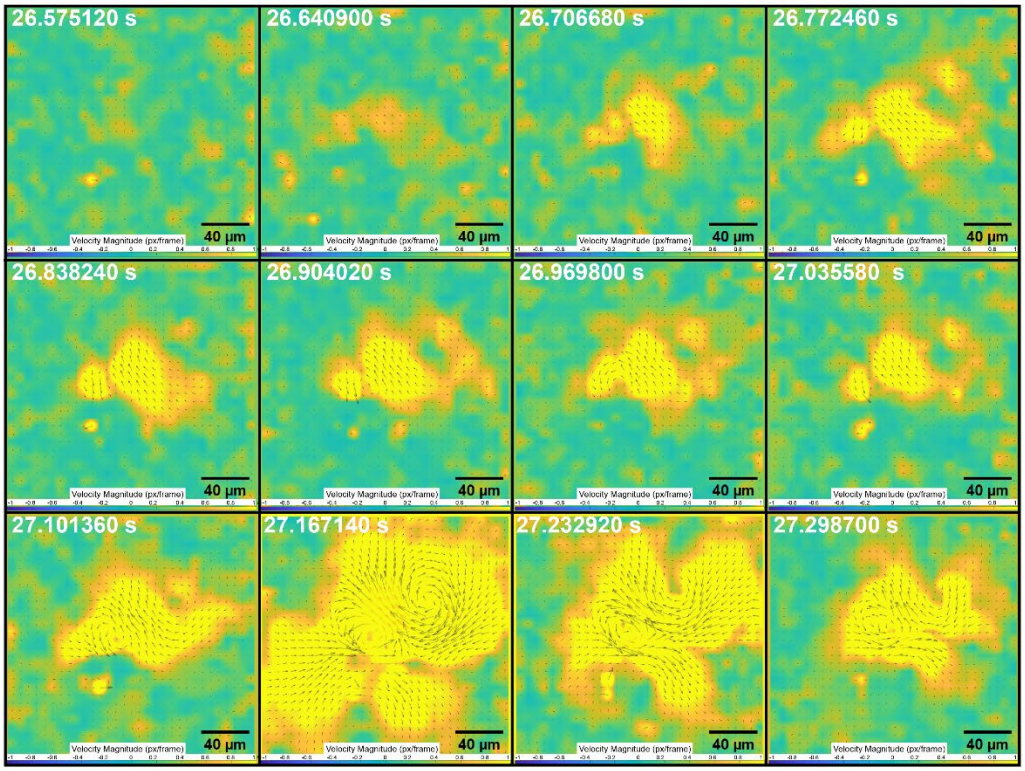

Fig. 7 PIV Analysis of Rotifer Movement in Gel Layer of Amoeba Chaos

Figure 7. PIV Analysis of Rotifer Movement in Gel Layer of Amoeba Chaos
7.1 Transmitted light time-lapse images showing the movement of a rotifer inside the gel layer of an amoeba treated with 1 μM Latrunculin B (LatB), a compound known to disrupt actin polymerization. Overlaid on the images are particle image velocimetry (PIV) vectors, which indicate the local flow patterns within the amoeba's cytoplasm as the rotifer moves. Time stamps for each frame are provided in seconds, and the scale bar represents 40 μm. 7.2 PIV vector overlays on heat maps representing vector magnitude in pixels per frame (px/frame). These heat maps show the velocity distribution in the surrounding cytoplasm as the rotifer moves, with warmer colors indicating higher velocity regions. The arrows illustrate the direction and magnitude of flow, with clear vortex-like structures appearing around the rotifer, especially in later frames. Each panel corresponds to the time stamps shown in S2.1, highlighting the dynamic interaction between the rotifer and the surrounding gel layer of the amoeba

Hyper Mixing Simulation of Beads

To study the effects of mid cell state switching on mixing we turn to simulations driven by our observations for gel and solution/liquid layers in the previous section, “Gel and Liquid State Observations”. In our simulation, the organization of gel and liquid state layers reflects amoeba morphology (**Fig. 3.1**, **Fig. 3.2**). However, we scale down the liquid and gel layers, representing them as three planes, each measuring 200 μm by 200 μm (**Fig. 8.1**).

Our simulation, referred to as hyper mixing, follows three core rules (**Fig 8.2**): (1) bead movement through stepping, (2) end switching, and (3) mid-cell switching. In the first step, beads take a step within their respective layers, with gel and liquid flows moving in opposite directions. For each bead in the solution/liquid state, an individual step is calculated for the X and Y component per time point. The distance for each step in the X component is generated by adding dx(BrownianMotion), calculated using the liquid state diffusion coefficient D, and dx(DirectedMotion), calculated using the liquid state mean velocity V. The same operation is applied to the Y component of beads in the liquid state. In the gel state, all beads take a uniform step at every time point since the entire gel layer moves like a conveyor belt with beads on it. Similarly, this X component of this step is generated by adding dx(BrownianMotion), calculated using the gel state diffusion coefficient D, and dx(DirectedMotion), calculated using the gel state mean velocity V. To accurately represent the conveyor belt properties of the gel layer we only added noise to the Y component of beads in the gel layer. This noise is generated by dimming the gel state diffusion coefficient D to 1% in our dx(BrownianMotion) calculation. Since the gel

state has a Pe of 212, indicating that its advection dominates with diffusion contributing minimally, we don't expect lateral diffusion in the Y direction to play a critical role in the gel layer. This also best reflects the confined movement of the bead's conveyor belt like movement, which is most likely driven by actin treadmilling at the cortex.

In the second step, beads switch layer states upon reaching the cell boundary (Y = 200 for liquid flow and Y = 0 for gel flow). Once they switch states, beads are assigned a dwell time, determining when they will switch layers again. In the third step, we model mid-cell switching by checking for expired dwell times, which triggers state changes. Each time a bead switches state, a new dwell time is then assigned, drawn from the distributions fit in **figure 6.5**, and the simulation advances to the next time point, repeating the cycle of these three core rules. At T0 the simulation is primed by assigning each bead a random dwell time.

To assess the impact of mid-cell switching, we ran the simulation without enabling the third core rule, referring to this simplified version as standard mixing, which only includes stepping and end switching. This version aligns with traditional views and observations reported of sol to gel transitions in amoeba [51, 25].

Visual results from both standard mixing and hyper mixing simulations show that hyper mixing significantly accelerates mixing compared to standard mixing (**Fig. 8.3**). To quantify this difference, we applied two mixing metrics: the Subdomain Mixing Index (SMI) and the Simple Nearest Neighbor (SNN) mixing score (**Fig 8.4**). The SMI calculates the weighted sum of fractions for two populations in fixed subdomains weighted by the total number of beads in each while the SNN measures the sum of fractions for each bead's five nearest neighbors. The Subdomain Mixing Index (SMI) is a reliable metric for determining when a system reaches stable mixing, as variations in subdomain size do not affect the point at which complete mixing is observed [16]. We developed the SNN to calculate the percentage of mixing without relying on fixed subdomains, which is particularly useful for amoebas that constantly change shape over time, making fixed subdomains impractical. Here our data shows that SMI and SNN both reach an asymptote at the

very similar times, showing that the SNN can be used as a reliable mixing metric to quantify mixing over time in subsequent applications (**Fig 8.4.1** and **Fig 8.4.3**).

In our standard mixing simulation, both SMI and SNN indicated stable mixing after 6 flow cycles (**Fig 8.4.1**). A flow cycle is defined as the time it takes for a bead to travel completely through the liquid layer and return via the gel layer. In our simulations, we add 1000 particles to X = 0 and use these extra particles to determine the average time it takes 1000 particles to complete 1 flow cycle (**Fig. 8.3.2**). Aside from mixing slowly, standard mixing also takes much longer to evenly spread beads (**Fig 8.3.2**, **Fig. 8.3.4**, **Fig. 8.3.5**, **Fig.8.4.2** and **Fig. 8.4.4**). Bead density analysis over time, measured using a central subdomain in each layer, revealed that beads remained clustered within their respective layers in standard mixing (**Fig 8.4.2**). In contrast, the hyper mixing simulation demonstrated complete mixing after just one flow cycle, with central subdomain density measurements showing that beads were evenly distributed after a single cycle (**Fig 8.4.3** and **Fig 8.4.4**). This is also apparent in **figure 8.3.2.**

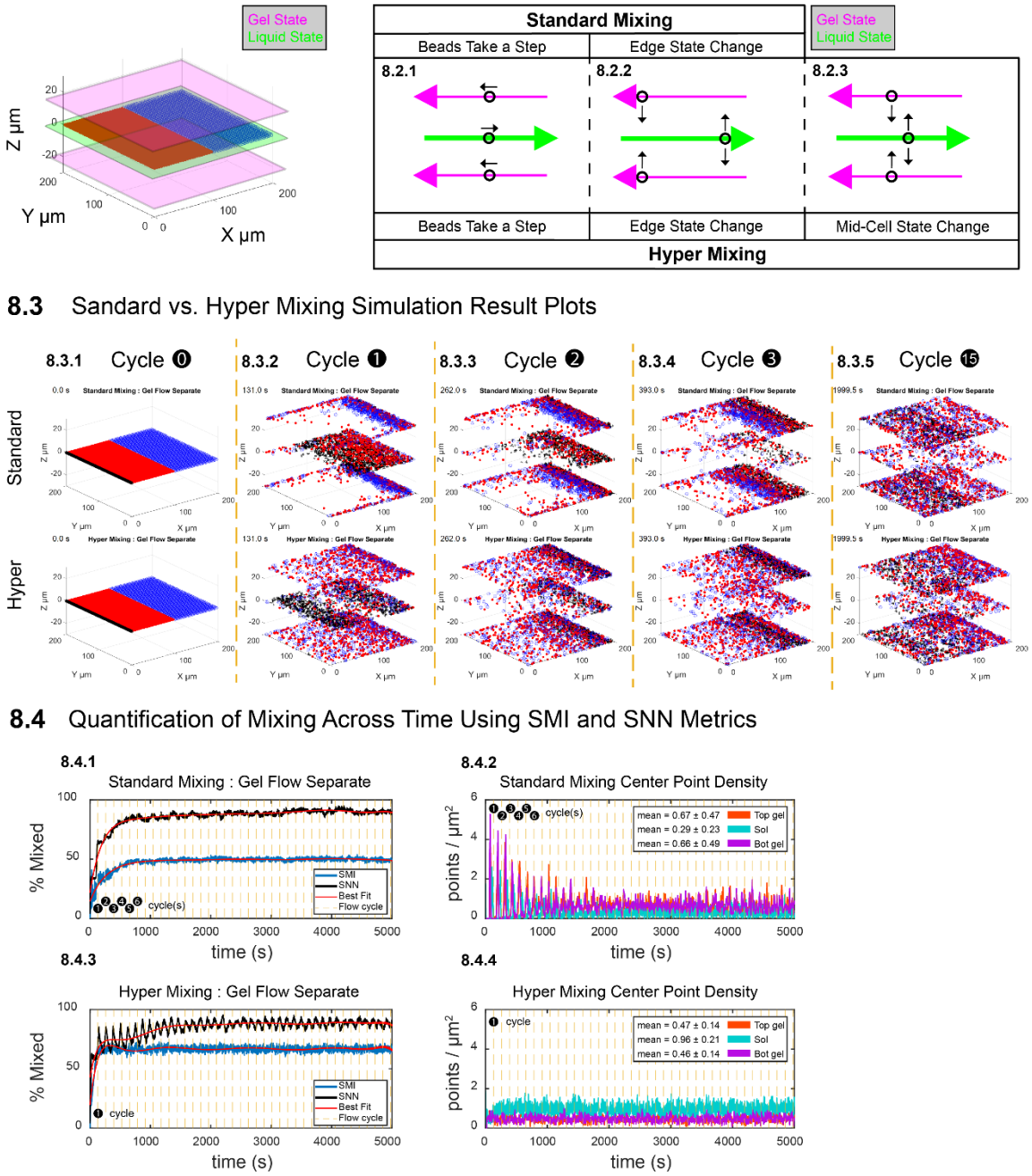

Fig. 8 Hyper Mixing Simulation

Figure 8. Hyper Mixing Simulation
8.1 3D simulation model: A 3D representation of the simulation space, showing the gel (magenta) and liquid (green) states across the X, Y, and Z axes. 8.2 Standard vs. Hyper Mixing Simulation Rules: 8.2.1–8.2.2 Standard mixing rules - beads take steps and change states at leading and trailing edges.

(Figure caption continued on the next page)

(Figure caption continued from previous page)

8.2.3 Hyper mixing rules - mid-cell state changes that allow more complex state transitions. 8.3 Standard vs. Hyper Mixing Simulation Result Plots: 8.3.1–8.3.5 Time Laps of Standard Mixing Simulation Results Plots. 8.3.6–8.3.10 Time Laps of Hyper Mixing Simulation Results Plots. 8.4 Quantification of Mixing Across Time Using SMI and SNN Metrics: 8.4.1 SMI and SNN comparison over time for standard mixing. 8.4.2 Standard mixing center point density across all 3 layers. 8.4.3 SMI and SNN comparison over time for hyper mixing, highlighting the increased mixing rate compared to standard mixing. 8.4.4 Hyper mixing center point density, showing a more even distribution of points across the cell layers compared to standard mixing. Red markers indicate complete flow cycles.

Hyper Mixing Simulation Validation via Experimental Delays

To validate the results of our hyper mixing simulation, we sought to test mixing experimentally. The SMI and SNN metrics depend on spatial observation between two or more distinct populations of beads. Conventionally, this would require microinjecting two bead populations with different labels into an amoeba, which is technically challenging. This approach demands two simultaneous on-scope injections and limits the study to observing a single mixing event post-injection (**Fig. 9.1**). To address these limitations, we developed an alternative strategy: we microinjected a single population of beads and then used image analysis to digitally split the population into two artificially colored groups. This method allowed us to initiate tracking of mixing events at any frame throughout the video, provided that all trajectories were continuous (**Fig. 9.2**).

Tracking beads continuously over long periods, up to 12 hours in this case, becomes increasingly difficult as bead populations become larger. For this reason, we only microinjected 18, 10 μm YG beads into our sample. Despite our reasonable bead population size we generated 54 total tracks, indicating that some tracks failed to maintain continuity and started new tracks to preserve accuracy. To overcome this limitation, we developed a custom MATLAB script that filtered through the 54 tracks to find video segments containing 18 continuous tracks. We then analyzed those individual video segments.

The longest continuous segment, consisting of 15,000 frames, captured 1 hour and 2.5 minutes of continuous mixing. From this segment, we calculated SNN scores across 10,000 mixing delays ranging from 0 to 5,000 seconds and plotted the results (**Fig. 9.4** and **Fig. 9.5**). We

did not use the SMI index for experimental data because of difficulty defining the sub-domains in a cell that constantly changes shape. Complete mixing, as judged by reaching the asymptotic value of the SNN plot, was achieved within 500 seconds in this cell. This is also how long it takes to complete a flow cycle in this cell.

To validate our hyper mixing simulation, we extracted liquid and gel state parameters—dwell times, diffusion coefficients, and mean velocities—from the same video segment used to calculate mixing across delays. We used the extracted gel and solution state parameters, including dwell time distributions in the sol and gel states, to run a hyper mixing simulation and compared the simulated SNN scores with the experimentally observed delay SNN scores across time. The resulting plots showed nearly identical lines between the simulation SMI and experimental SNN (**Fig. 9.5**), and a similar trend between simulation SNN and experimental SNN, confirming that our simulations accurately reflected the experimental mixing behavior found in the amoeba's cytoplasm. We emphasize that our model does not involve fitting any free parameters to the SNN curve - all parameters of the model were measured experimentally from bead tracking data. Ultimately, this method allowed us to study mixing both indirectly via hyper mixing simulations and directly through digital experimental mixing across delay intervals.

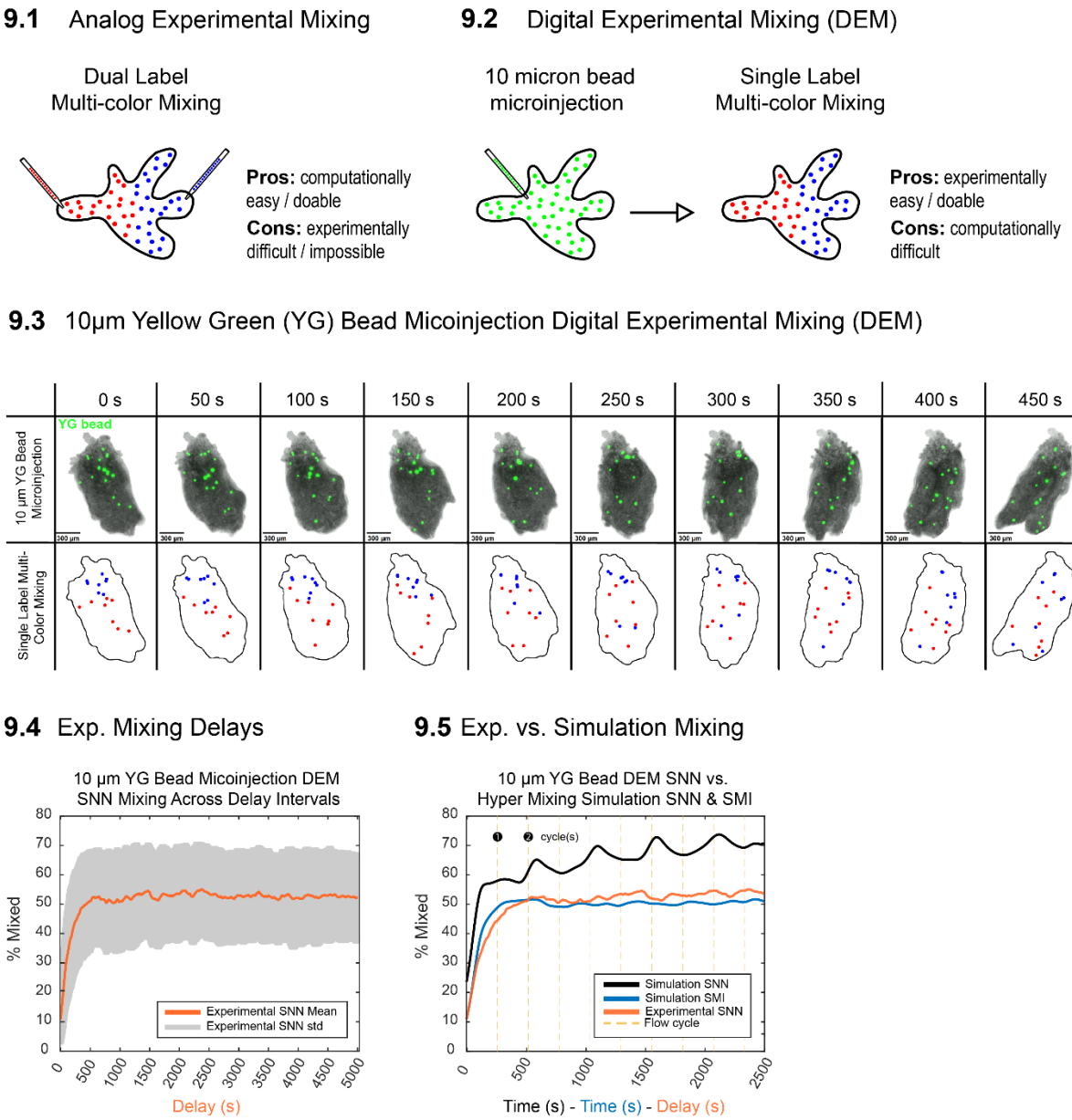

Fig. 9 Experimental Mixing vs. Simulation Mixing

Figure 9. Experimental Mixing vs. Simulation Mixing
9.1 Analog experimental mixing using dual label multi-color mixing. Pros and cons are noted: computationally easy but experimentally difficult. 9.2 Digital experimental mixing (DEM) using 10 µm bead microinjection. This method uses a single label to establish multi-color mixing. Pros and cons are noted: experimentally easy but computationally challenging. 9.3 Time-lapse images showing the digital experimental mixing (DEM) process using 10 µm YG bead microinjection. Bead movement is tracked over 450 seconds, and the bottom row illustrates single label multi-color mixing in corresponding frames. 9.4 Diagram to show Simple Nearest Neighbor (SNN) calculations are performed across different delay frames (1s, 2s, 3s, and up to 5000s delay). 9.5 Expression for the SNN mean, where d is the delay and N is the total number of frames (15000).

(Figure caption continued on the next page)

(Figure caption continued from previous page)

9.6 DEM SNN calculations across time delays. The plot shows the percentage mixed as a function of delay, with mean and standard deviation indicated. 9.7 Comparison of DEM SNN with Hyper Mixing Simulation SNN: The plot compares the experimental SNN with simulated SNN for hyper mixing, showing similar mixing behavior between exp. l and sim. results.

Hyper Mixing Simulation of Nuclei

To confirm that the mixing results obtained with beads reflect the dynamics experienced by actual organelles, we repeated our analysis using nuclei instead of beads to track flow and measure mixing. It is well known that amoebas can contain many nuclei, sometimes numbering in the hundreds per cell [26]. Nuclei in amoeba chaos are reported to be around 19 μm in diameter [13], which is why we chose to use 20 μm beads in our initial experiments. The large number of nuclei makes it technically challenging to track them, since their tracks will frequently overlap. To improve our ability to track nuclei over time, we designed an assay to sparsely label nuclei using Histone H1-488 protein microinjection (**Fig. 10** and **Fig. 11.1**). Unlike uniform labeling methods like DNA dyes (e.g., Spy 650), we found that when Histone H1-488 is injected into cells, it is transported into nuclei heterogeneously, causing nuclei to be labelled at varying intensity levels (**Fig. 10**). By focusing on tracking only the brightest nuclei, we effectively reduce the density of nuclei being tracked. However, we still generate thousands of tracks per experiment since the brightest nuclei are significantly dimmer than 10 μm or 20 μm YG beads used in previous sections.

Despite the reduced density, tracks frequently end causing new ones to form when nuclei move out of the focal plane (e.g., moving away from the coverslip) since they are so dim. Tracking can also be affected when nuclei intersect many other dimly lit nuclei. This makes continuous tracking across long time periods challenging. To address the issue of shorter track lengths compared to those analyzed in previous sections, we modified our MATLAB script to extract parameters for the hyper mixing simulation without requiring tracks to be continuous for the entire video length. Instead, we set a cut off for minimum track length and analyzed all tracks for dwell states using an MSD threshold, as done in previous sections. With thousands of tracks to

consider, it became especially important to trim the first and last dwell state events in each track, since we cannot determine the full duration of those events. From these trimmed tracks, we classify nuclei as gel or liquid state based on MSD. We also use these trimmed tracks to calculate gel and liquid state dwell time distributions (**Sup. Fig S4**).

Our hyper mixing simulation results for nuclei (**Fig. 11.2** and **Fig. 11.3**) were consistent with those for 10 μm and 20 μm beads in the previous sections. We found that nuclei mixing was completed in one cycle (**Fig. 11.3**), with both the SMI and SNN metrics stabilizing around the same time. The only difference between bead and nuclei simulations was the distribution used to model dwell time in the gel layers. Gel state dwell time was modeled using an inverse gaussian distribution in bead simulations whereas a Birnbaum-Saunders distribution was used to model gel state dwell time in nuclei simulations.

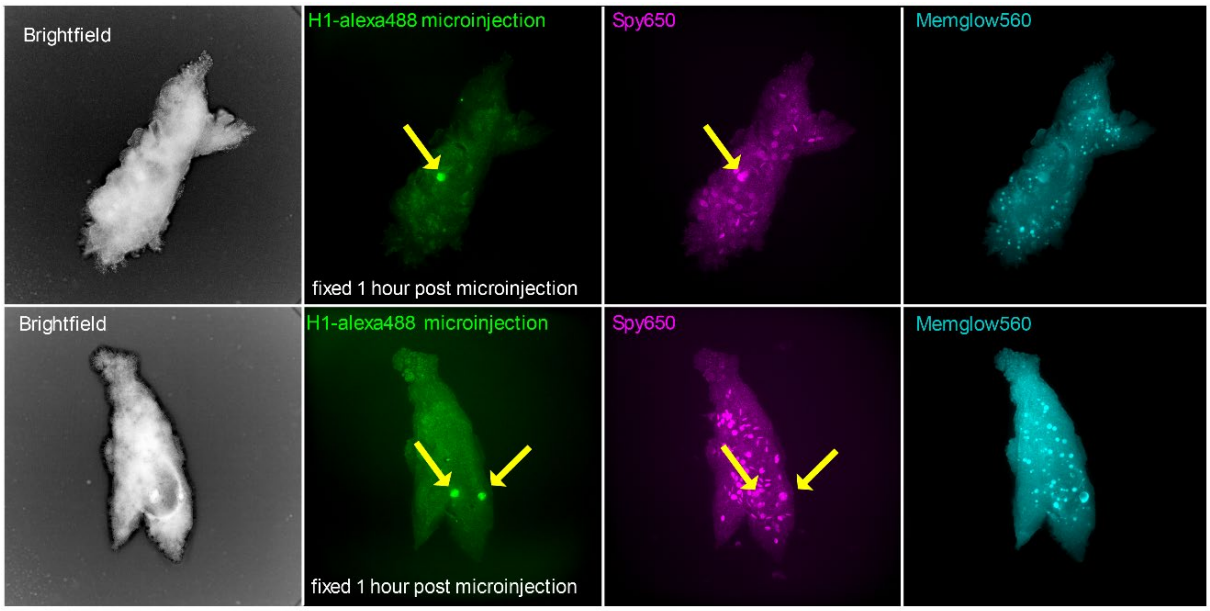

Fig. 10 Using Histone H1-488 Microinjection for Sparse Nuclei Labeling

Figure 10. Using Histone H1-488 Microinjection for Sparse Nuclei Labeling
This figure illustrates the results of microinjection of Histone H1-Alexa488 for sparse labeling of nuclei in cells. The brightfield images (left column) show the overall morphology of the cells, while the fluorescence images (middle columns) display nuclei labeled with H1-Alexa488 (green), Spy650 (magenta), and Memglow560 (cyan). Yellow arrows indicate specific nuclei labeled with H1-Alexa488 and Spy650 in both time points, taken 1 hour post-microinjection. The H1-Alexa488 signal is localized to the injected nuclei. The overlap between Spy650 and H1-Alexa488 demonstrates colocalization in specific nuclear regions.

11.1 H1-488 Microinjection time lapse - n1

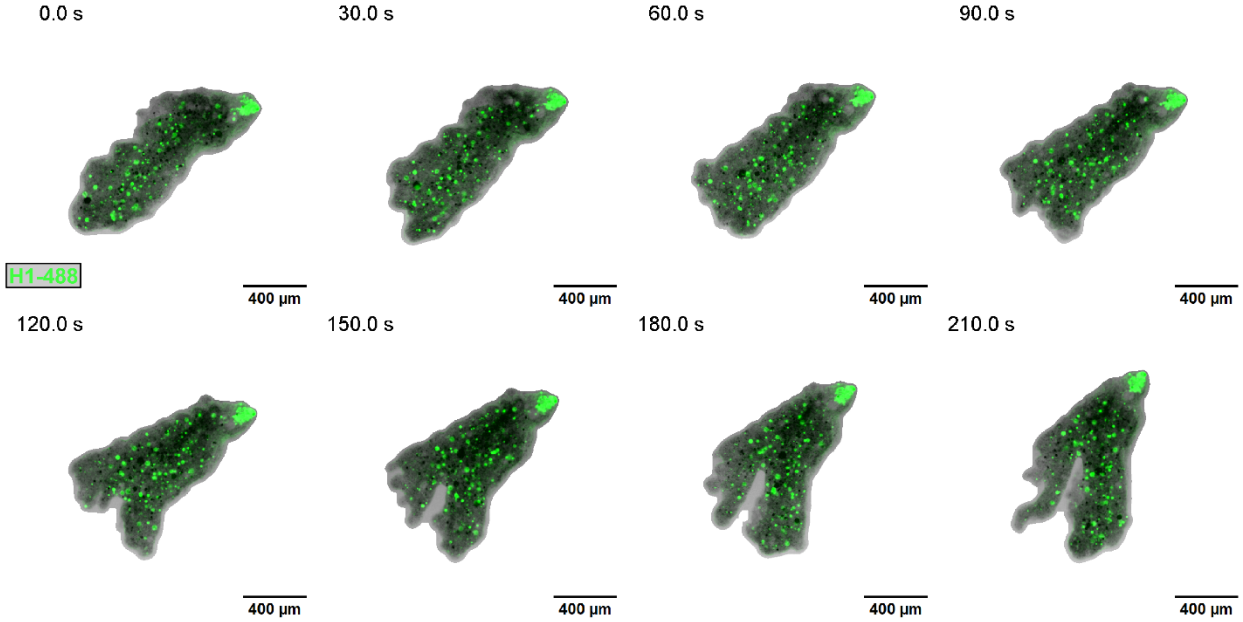

11.2 Hyper Mixing Simulation - n1

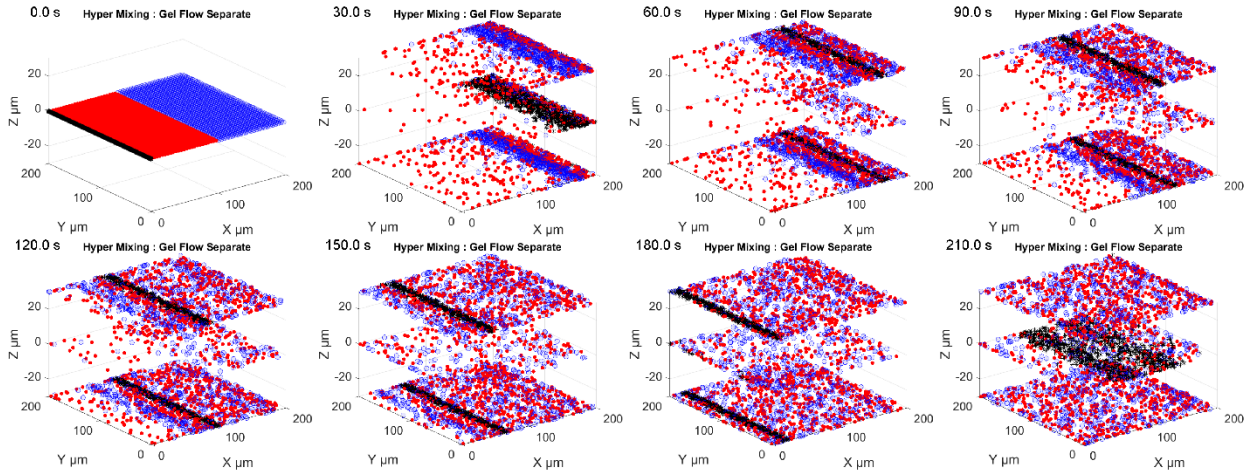

11.3 Hyper Mixing Simulation Quantification Across Time - n1

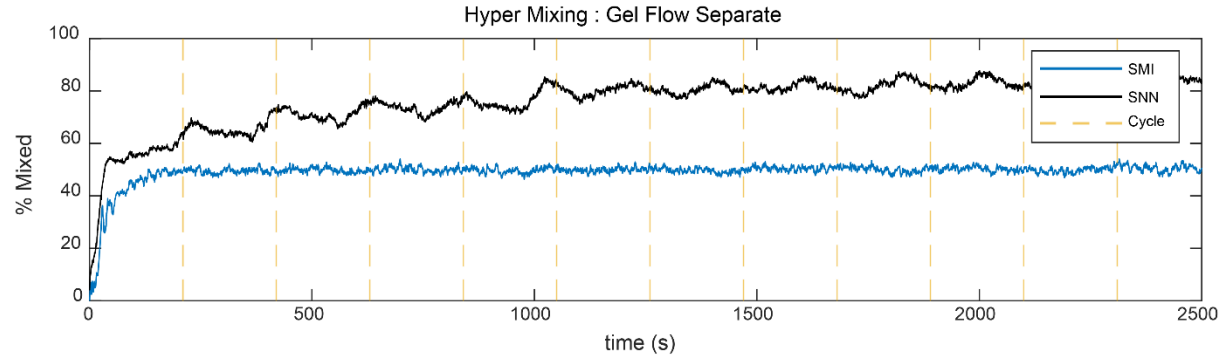

Fig. 11 Mixing of Nuclei - Histone H1-488 n1 of 4

Figure 11. Mixing of Nuclei – Histone H1-488 n1 of 4
11.1 Fluorescence time lapse panel of histone H1-488 microinjected into amoeba. A 30 second interval is given between frames and each frame has a scale bar of 400 μm. **11.2** Gel and liquid state hyper-mixing simulation: **11.3** Simulation results of SMI and SNN mixing across time. The plot shows the percentage of mixed nuclei over time, comparing the Subdomain Mixing Index (SMI) and Spatial Nearest Neighbors (SNN) metrics, demonstrating consistent mixing behavior over a 2500-second period.

All four Histone H1-488 samples reach a stable mixing state in 1 flow cycle, which took an average of 136 seconds across all four samples (**Fig 12.1** and **Fig 12.2**). This was surprising considering that sample n1 had a liquid state flow over 80 percent slower than the rest of the samples. This is reflected in the significantly lower diffusion coefficient of 40.2 $\mu m/s^2$ in sample n1 compared to 182 $\mu m/s^2$, 180 $\mu m/s^2$, and 217 $\mu m/s^2$ in samples n2 n3 and n4 (**Sup. Fig. S4, Sup. Fig. S6**, **Sup. Fig. S8**, **Sup. Fig. S10**). The diffusion coefficients for the gel layer were 6.39 $\mu m/s^2$,14.5 $\mu m/s^2$, 25.4 $\mu m/s^2$, and 15.1 $\mu m/s^2$ for samples n1, n2, n3, and n4. Despite our observed range of solution/liquid and gel state diffusion coefficients, each amoeba crawled at relatively similar speeds, ~ 6 μm/s (**Fig12.5**). The amoeba with the slowest liquid and gel diffusion coefficients, sample n1, was also the largest cell of the 4 (**Fig 12.6**). The flow system across the liquid and gel layers demonstrates remarkable versatility, not only achieving a stable mixing state across samples with varying diffusion coefficients but also maintaining consistent cell crawling speeds. This consistency in crawling speed, despite differences in diffusion and flow rates, highlights the adaptability of the flow mechanism in facilitating both effective mixing and stable locomotion across diverse physical states. The ability of even slower-flowing samples like n1 to reach comparable crawling velocities suggests that the system compensates for diffusion variability, ensuring reliable performance in both mixing and cellular movement.

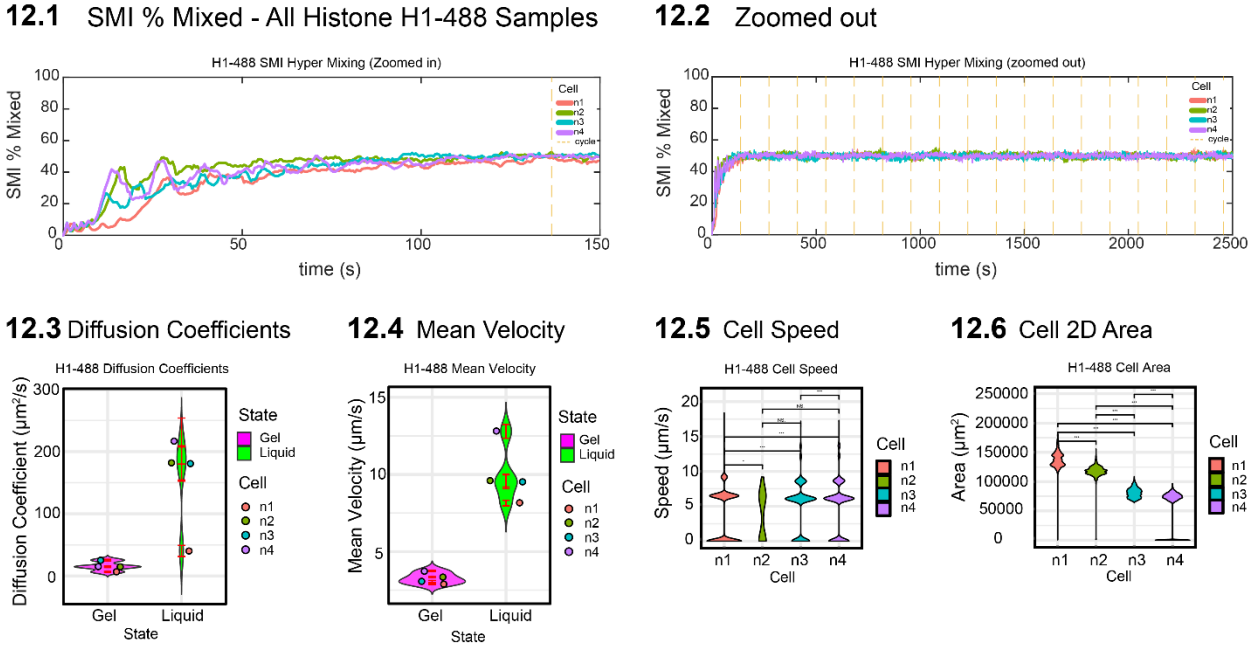

Fig. 12 Mixing of Nuclei is Independent of Diffusion Constant

Figure 12. Mixing of Nuclei is independent of Diffusion Constant
12.1 SMI (% mixed) over time for all Histone H1-488 samples. The plot shows the subdomain mixing index (SMI) for four different cells (n1, n2, n3, n4), indicating the degree of mixing as a percentage over time. 12.2 Zoomed-out view of the SMI % mixed over an extended period, showing long-term mixing stability across all four cells. 12.3 Diffusion coefficients for the gel (magenta) and liquid (green) states in cells n1 to n4. 12.4 Mean velocity comparison between gel and liquid states in the four cells. 12.5 Cell crawling speed for each cell (n1 to n4) shown in a violin plot. Significant differences between the cells are indicated using asterisks. 12.6 2D cell area for cells n1 to n4, demonstrating the variation in cell size, with statistically significant differences indicated using asterisks.

DISSCUSSION

In both the ballistic and super-ballistic regimes, systems exhibit high to very high mixing efficiency, and the potential for complete mixing within one cycle is strong, particularly in the super-ballistic regime where particle separation happens at an increasingly rapid rate [41]. However, In the super-diffusive regime, while high mixing efficiency is observed, complete mixing in a single cycle is unlikely, and even more unlikely in the sub-diffusive regime. In super-diffusive regimes, particles will explore a large part of the system in a relatively short time, but the process is not as thorough as it would be in ballistic or super-ballistic regimes, where complete mixing is more probable within one cycle. Despite over 90% of our observations falling in the super-diffusive and sub-diffusive regimes, our data indicates that amoeba reaches complete mixing within one flow cycle. From an ergodic hierarchy perspective, amoeba hyper mixing is a Bernoulli system, which is the fastest type of mixing known. This observation suggests that amoeba may have evolved a way to use laminar flows to achieve super-ballistic mixing results; one of the advantages active matter mixing systems possess over mixers made using conventional materials and strategies.

Our measurements do not support our original idea of a pseudopod-based Baker's transform. The timescale of mixing, as fast as 88 seconds (**Sup. Fig. S7**) is faster than the timescale of pseudopod formation which roughly takes 200 seconds. Moreover, when pseudopod number was altered in our samples (**Fig. 5**), it did not significantly affect bead separation rates or power law exponents, suggesting that pseudopod generation alone does not directly influence mixing efficiency. This contradicts the intuitive notion that more pseudopods lead to faster or more efficient intracellular mixing. In a broader context, this is particularly important because several different species of amoeba lack the ability to form pseudopods while other naturally produce more pseudopods, such as the amoeba chaos used in this study. In addition, it’s possible that other systems lacking pseudopods but possessing gel and liquid state cytoplasm, along with

laminar flows, such as the slime mold, may also intracellularly mix using a similar strategy to the one reported in this work.

The sol to gel transition occurs across the entire cell body, particularly at the leading and trailing edges, as previously reported. While the mechanism controlling this transition remains unclear, our study highlights a novel characteristic: mid-cell sol to gel switching. We know that gel transforms into sol state at the uropod (rear) and sol transitions into gel at the hyaline cap (front). We also know that in the gel state, the actin network is densely packed into thick filaments, while in the sol state, it becomes loosely organized into sparse, thin filaments.

The complete assembly and disassembly of this network at the front and rear may explain the sol to gel transition at the cell's edges, but it does not account for the newly observed mid-cell switching. Since the cortical actin network treadmills along with the gel layer from the leading to the trailing edge, we hypothesize that structural fatigue accumulates as the network travels between 1200 μm ~ 2000 μm, depending on the shape of the amoeba, from the hyaline cap to the uropod. This fatigue could lead to breaks in the network, which are subsequently repaired through self-assembly, possibly driving mid-cell sol to gel transitions and resulting in mid-cell cytoplasmic and bead state exchanges.

Supporting this hypothesis, we found that the Birnbaum-Saunders distribution, commonly known as the fatigue life distribution, best fits the experimental gel state dwell times in our nuclei experiments. This distribution, typically used to model the time until failure in materials subjected to cyclic or repeated stress, suggests that the actin cytoskeleton may experience fatigue and periodic self-repair as it treadmills from front to rear. This process could explain the unique mid-cell sol to gel transitions observed and may highlight the unforeseen advantages of structural fatigue when traveling across long distances.

To further investigate this possibility, future studies will aim to use live-cell fluorescence microscopy to visualize the actin cytoskeleton alongside bead dynamics, offering potential insights into this fatigue driven transition.

CONCLUSION

Our study provides detailed insights into the intracellular mixing dynamics within amoeba *Chaos* by utilizing both experimental and simulation-based approaches. Through the analysis of close bead pair separation events, we identified that most events fell within the sub-diffusive and super-diffusive regimes, with only a small fraction in the super-ballistic regime. These findings suggest that the amoeba's cytoplasmic flow should at most support moderate mixing behaviors. The lack of significant turbulent flow or explosive mixing events further highlights the controlled nature of amoeboid cytoplasmic streaming. However, when examining how mid-cell switching influences mixing, we discovered that amoeba is capable of complete mixing within one cycle, creating a Bernoulli system which is otherwise expected to arise from super-ballistic bead separation instead of the observed sub-diffusive and super-diffusive regimes.

We also demonstrated that increasing pseudopod number did not significantly enhance bead pair separation rates, suggesting that pseudopod generation alone may have a minimal impact on cytoplasmic mixing efficiency. This insight contributes to our understanding of how amoeboid motility and mixing may not be directly correlated with pseudopod formation but rather with other internal dynamics such as the sol to gel state transition.

By looking at mixing across delays in experimental data we validated our hyper mixing simulation and by extension the results generated from these simulations. Both simulated and experimental mixing shows that complete mixing can be achieved in a single flow cycle for both beads and nuclei. This consistency between experimental and simulated data across multiple sample types further supports the robustness of our approach. Interestingly, the variation in gel state dwell time distributions between beads and nuclei highlights subtle biological differences in regulation of their movement, particularly in the gel layer.

Ultimately, our findings provide a novel method to study mixing in amoeboid cells both experimentally and through simulations, offering a reliable framework for future investigations into

cytoplasmic dynamics and mixing efficiency in other cellular systems. Our study also opens avenues for exploring the role of biomechanical properties, such as diffusion coefficients and cell size, in determining the efficiency of intracellular mixing processes. This work paves the way for further research into how cellular environments can modulate cytoplasmic mixing, with potential applications in understanding intracellular transport and distribution of organelles and macromolecules in various cell types.

SUPPLEMENTARY FIGURES

S1.1 20µm Yellow Green (YG) Fluorescent Bead Microinjection in Amoeba Chaos n2

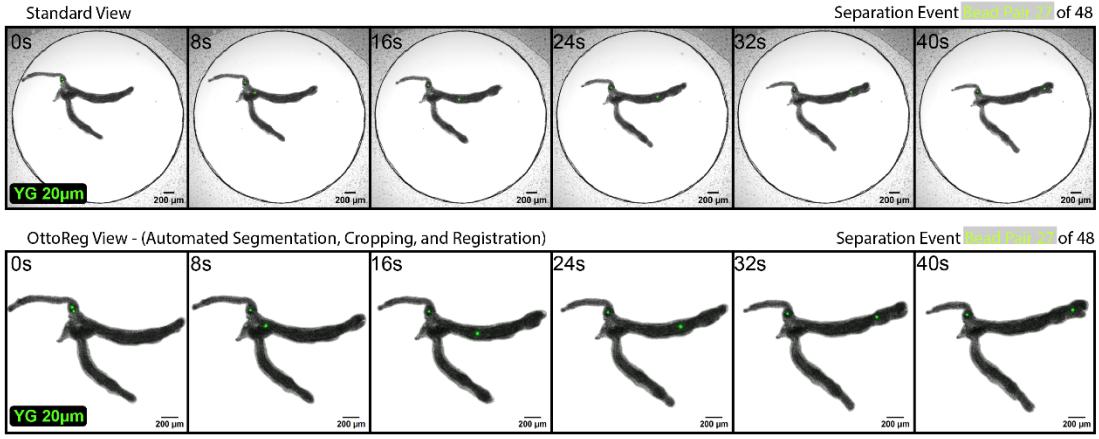

S1.2 Inter Partical Distance Over Time n2

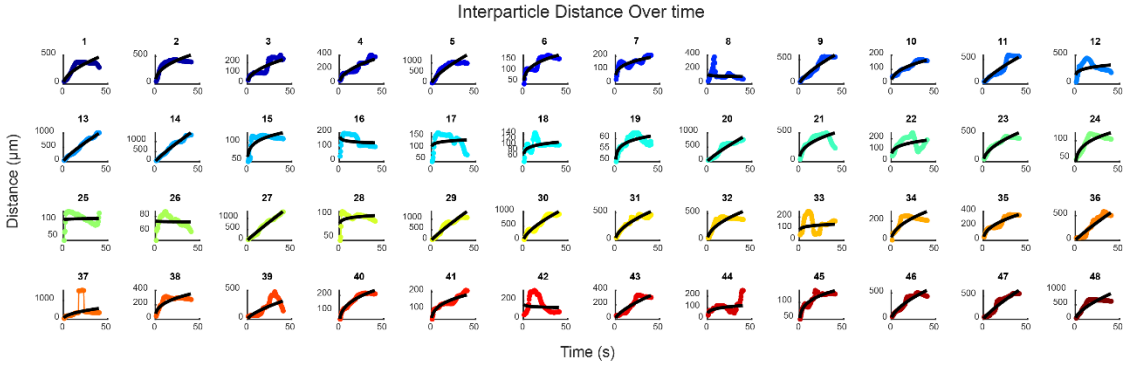

S1.3 Power Law Exponent for Time with Respect to Interparticle Distance n2

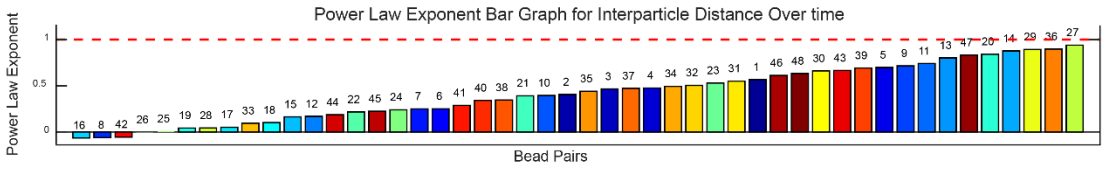

S1.4 Mean Squared Displacement for Bead Pair Trajectories n2

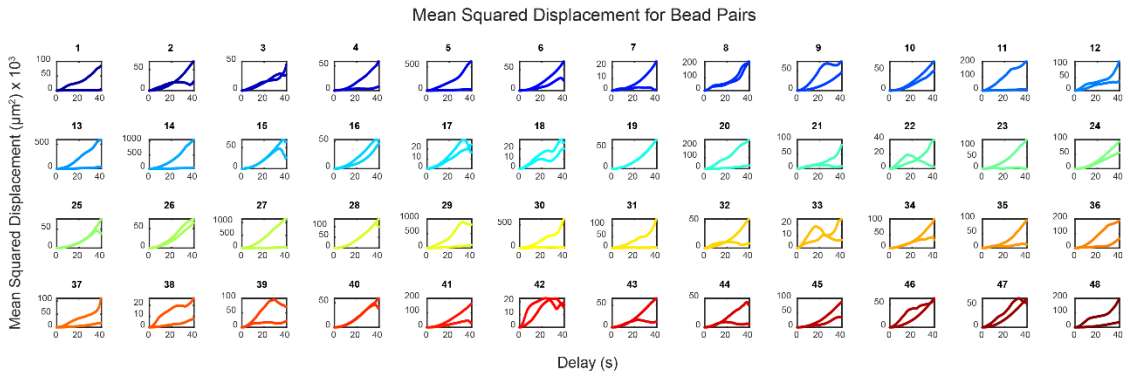

Fig. S1 20µm Bead Separation Assay n2 of 4

Figure S1. 20 μm Bead Separation Assay n2 of 4
S1.1 Time-lapse images showing the microinjection of 20 μm yellow-green (YG) fluorescent beads into Amoeba *Chaos*. The top row presents the standard view, and the bottom row shows the OttoReg view, where automated segmentation, cropping, and registration have been applied. The images capture a separation event for bead pair 21, showing the displacement of the beads over a 40-second time window. Scale bars represent 200 μm. S1.2 Interparticle distance over time for bead pairs tracked in the experiment. Each plot corresponds to a unique bead pair, displaying the distance (μm) between beads over time (s). S1.3 Power law exponent for interparticle distance as a function of time. The bar graph shows the power law exponent for each bead pair, with values color-coded and labeled. The red dashed line at Y = 1. S1.4 (MSD) plots for each bead pair trajectory. These plots show the MSD (μm^2) as a function of delay time (seconds), providing insight into the diffusion behavior of the beads within the amoeba.

S2.1 20µm Yellow Green (YG) Fluorescent Bead Microinjection in Amoeba Chaos n3

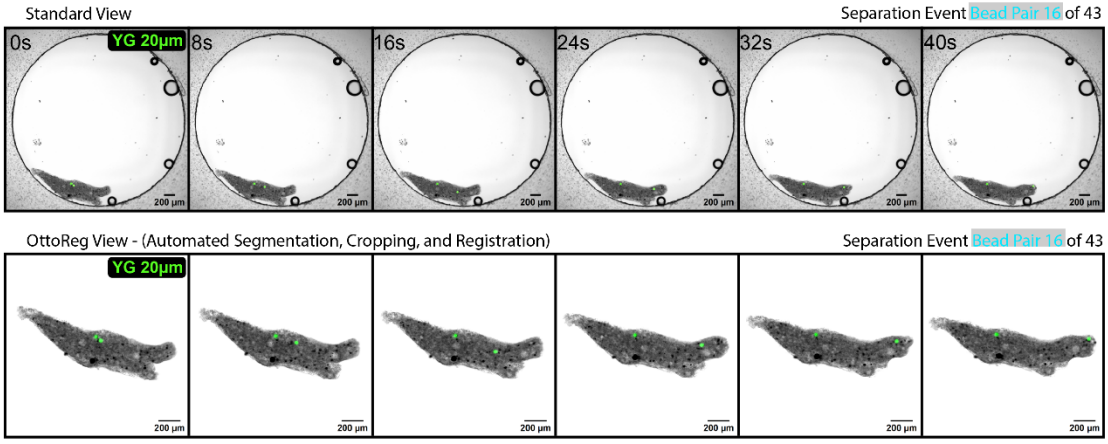

S2.2 Inter Partical Distance Over Time n3

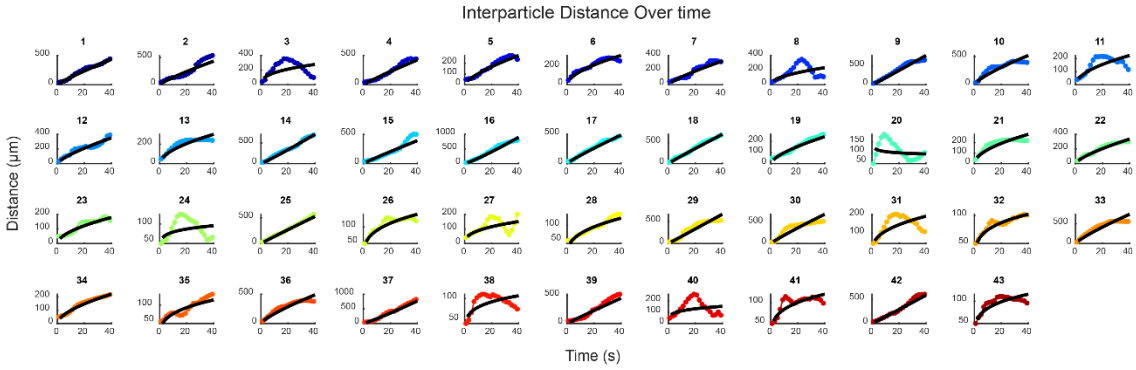

S2.3 Power Law Exponent for Time with Respect to Interparticle Distance n3

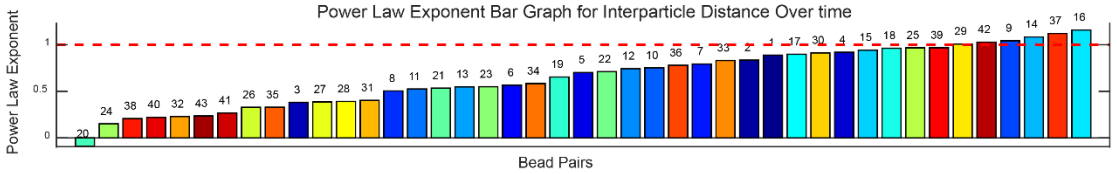

S2.4 Mean Squared Displacement for Bead Pair Trajectories n3

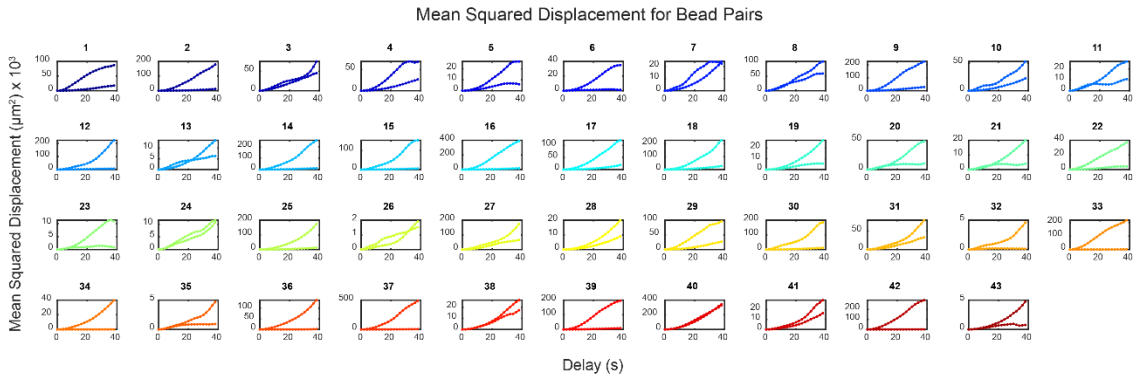

Fig. S2 20µm Bead Separation Assay n3 of 4

Figure S2. 20 μm Bead Separation Assay n3 of 4
S2.1 Time-lapse images showing the microinjection of 20 μm yellow-green (YG) fluorescent beads into Amoeba *Chaos*. The top row presents the standard view, and the bottom row shows the OttoReg view, where automated segmentation, cropping, and registration have been applied. The images capture a separation event for bead pair 16, showing the displacement of the beads over a 40-second time window. Scale bars represent 200 μm. S2.2 Interparticle distance over time for bead pairs tracked in the experiment. Each plot corresponds to a unique bead pair, displaying the distance (μm) between beads over time (s). S2.3 Power law exponent for interparticle distance as a function of time. The bar graph shows the power law exponent for each bead pair, with values color-coded and labeled. The red dashed line at Y = 1. S2.4 (MSD) plots for each bead pair trajectory. These plots show the MSD (μm^2) as a function of delay time (seconds), providing insight into the diffusion behavior of the beads within the amoeba.

S3.1 20µm Yellow Green (YG) Fluorescent Bead Microinjection in Amoeba Chaos n4

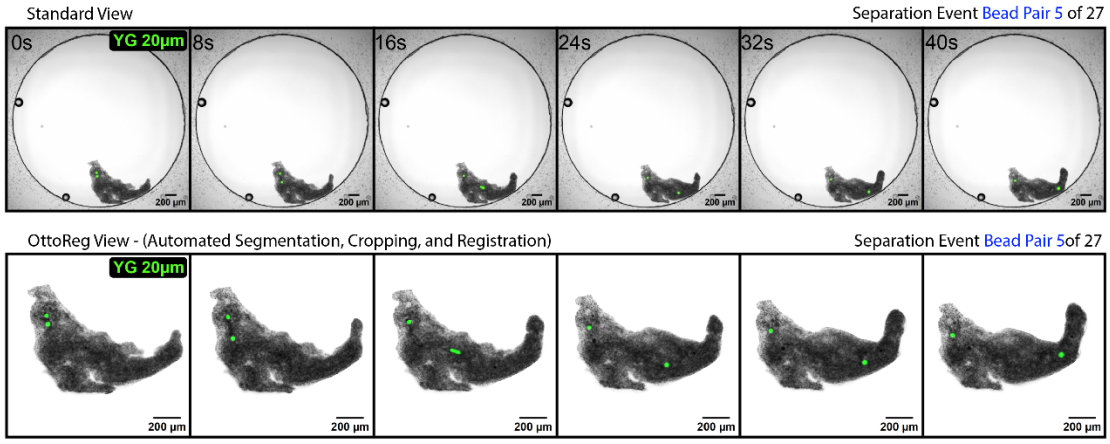

S3.2 Inter Partical Distance Over Time n4

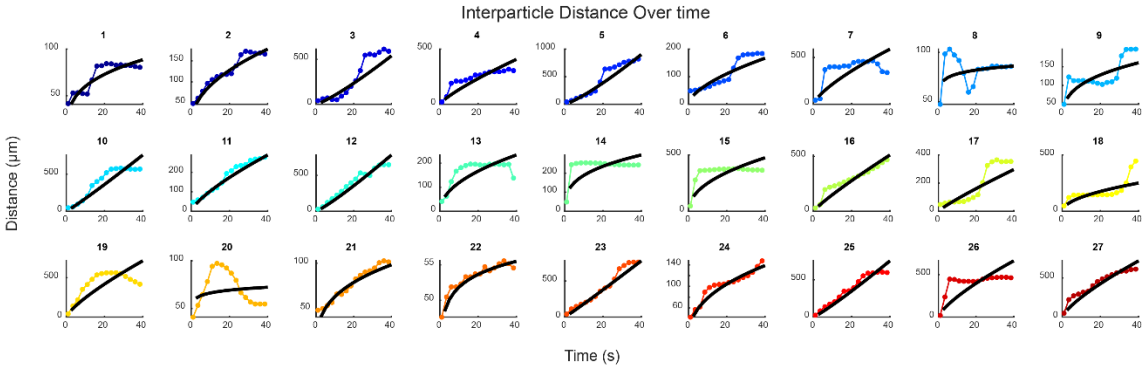

S3.3 Power Law Exponent for Time with Respect to Interparticle Distance n4

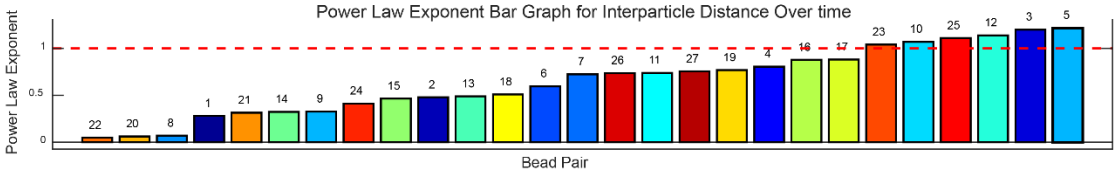

S3.4 Mean Squared Displacement for Bead Pair Trajectories n4

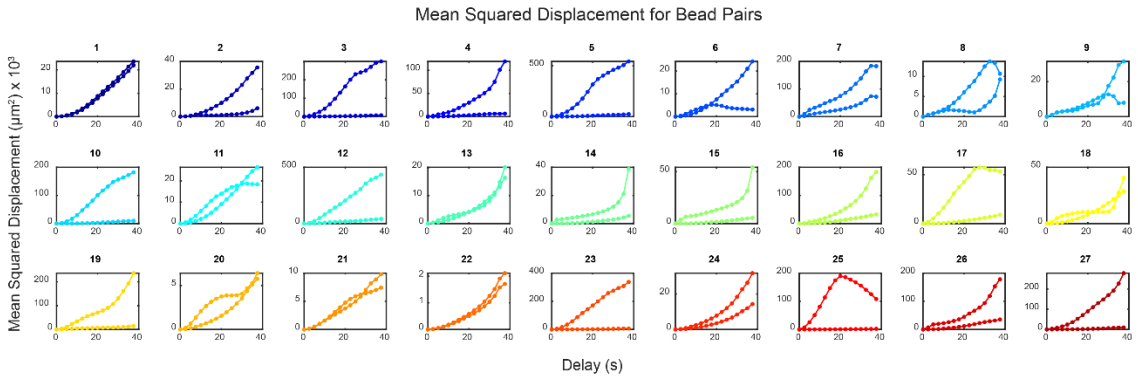

Fig. S3 20µm Bead Separation Assay n4 of 4

Figure S3. 20 µm Bead Separation Assay n4 of 4
S3.1 Time-lapse images showing the microinjection of 20 µm yellow-green (YG) fluorescent beads into Amoeba *Chaos*. The top row presents the standard view, and the bottom row shows the OttoReg view, where automated segmentation, cropping, and registration have been applied. The images capture a separation event for bead pair 5, showing the displacement of the beads over a 40-second time window. Scale bars represent 200 µm. S3.2 Interparticle distance over time for bead pairs tracked in the experiment. Each plot corresponds to a unique bead pair, displaying the distance (µm) between beads over time (s). S3.3 Power law exponent for interparticle distance as a function of time. The bar graph shows the power law exponent for each bead pair, with values color-coded and labeled. The red dashed line at Y = 1. S3.4 (MSD) plots for each bead pair trajectory. These plots show the MSD (µm²) as a function of delay time (seconds), providing insight into the diffusion behavior of the beads within the amoeba.

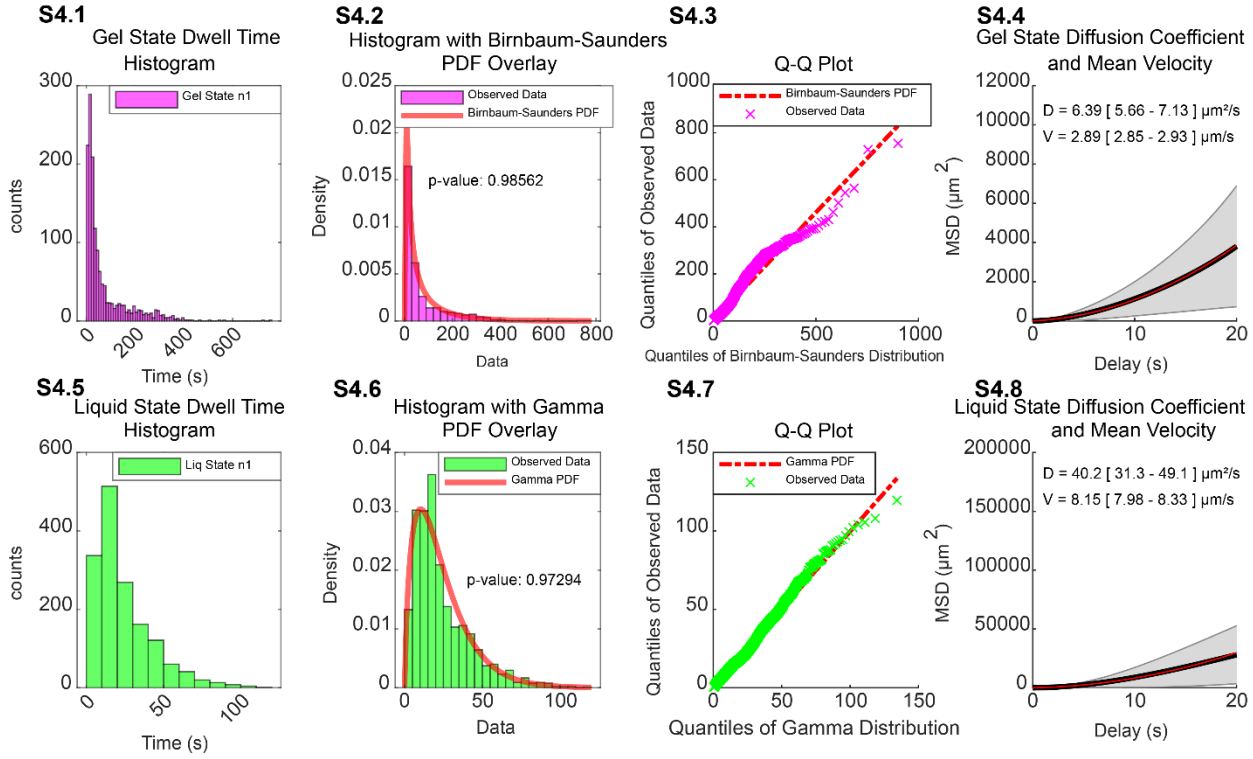

Fig. S4 Gel and Solution State Parameters - Histone H1-488 n1 of 4

Figure S4. Gel and Sol parameters H1-488 n1 of 4
S4.1. Gel state dwell time histogram, showing the frequency of dwell times for the gel state. S4.2 Histogram with Birnbaum-Saunders probability density function (PDF) overlay for gel state dwell times. S4.3 Q-Q plot comparing observed gel state dwell times with the Birnbaum-Saunders distribution. S4.4 Gel state diffusion coefficient (D) and mean velocity (V) derived from MSD analysis. S4.5 Liquid state dwell time histogram, showing the frequency of liquid state dwell times. S4.6 Histogram with Gamma PDF overlay for liquid state dwell times. S4.7 Q-Q plot comparing observed liquid state dwell times with the Gamma distribution. S4.8 Liquid state diffusion coefficient (D) and mean velocity (V) derived from MSD analysis.

S5.1 H1-488 Microinjection time lapse - n2

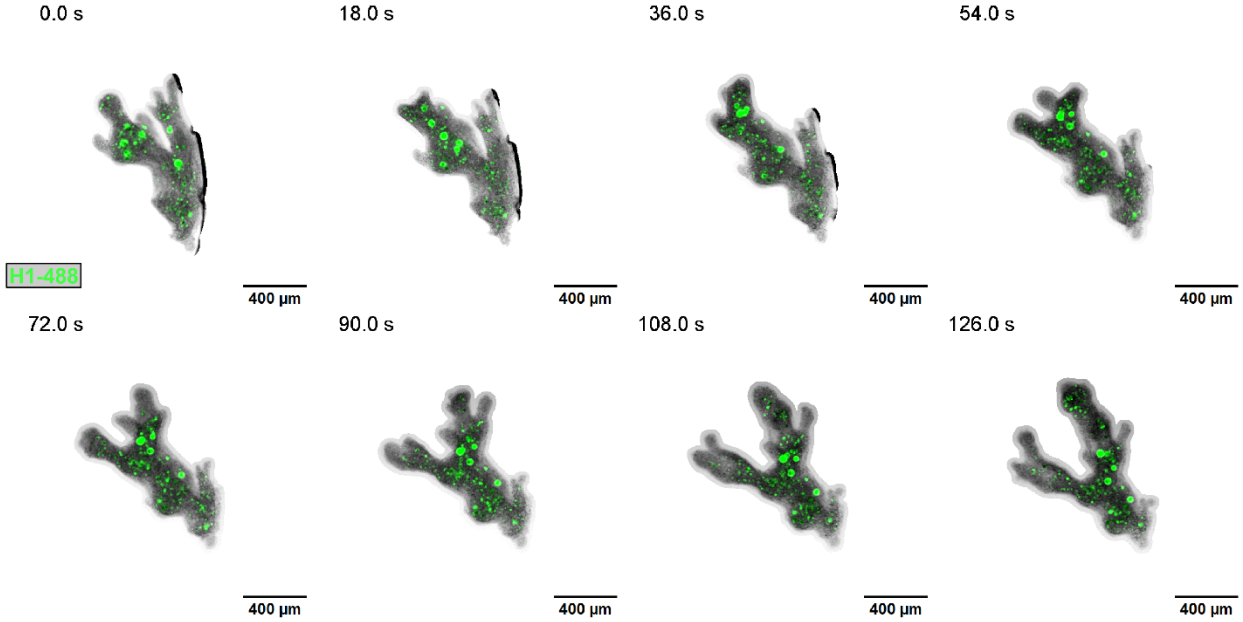

S5.2 Hyper Mixing Simulation - n2

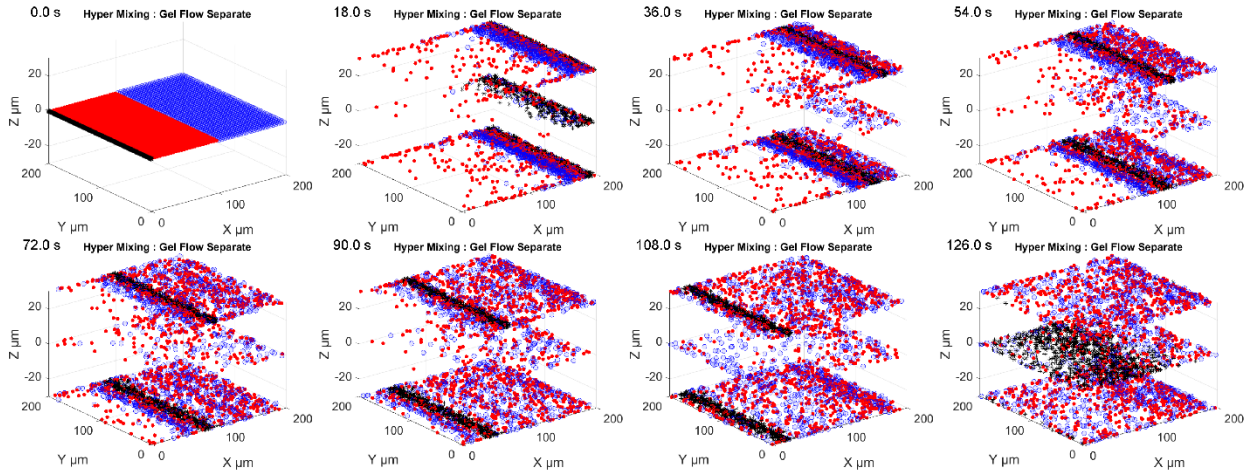

S5.3 Hyper Mixing Simulation Quantification Across Time - n2

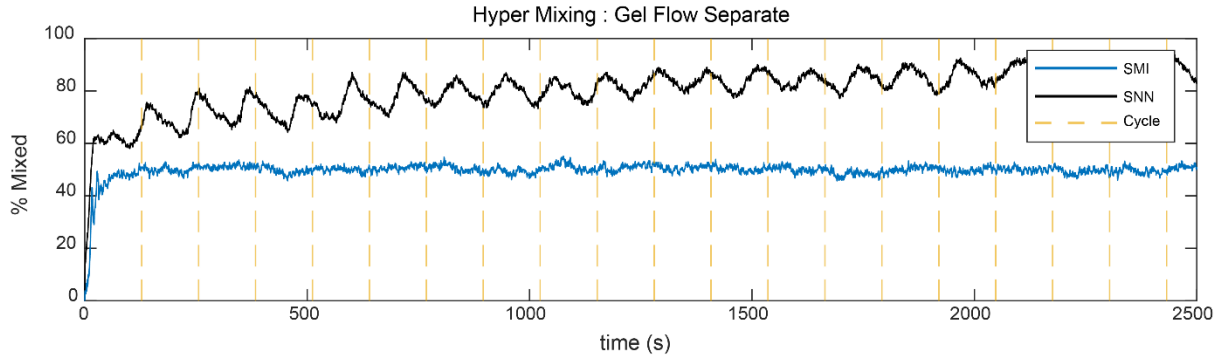

Fig. S5 Mixing of Nuclei - Histone H1-488 n2 of 4

Figure S5. Mixing of Nuclei – Histone H1-488 n2 of 4
S5.1 Fluorescence time lapse panel of histone H1-488. Mean squared displacement (MSD) threshold used to identify gel and liquid state localization in the nuclei labeled with Histone H1-488. Gel (magenta) and liquid (green) bead flow state is represented in the timelapse panel. S5.2 Gel and liquid state hyper-mixing simulation. S5.3 Simulation results of SMI and SNN mixing across time. The plot shows the percentage of mixed nuclei over time, comparing the Subdomain Mixing Index (SMI) and Spatial Nearest Neighbors (SNN) metrics, demonstrating consistent mixing behavior over a 2500-second period

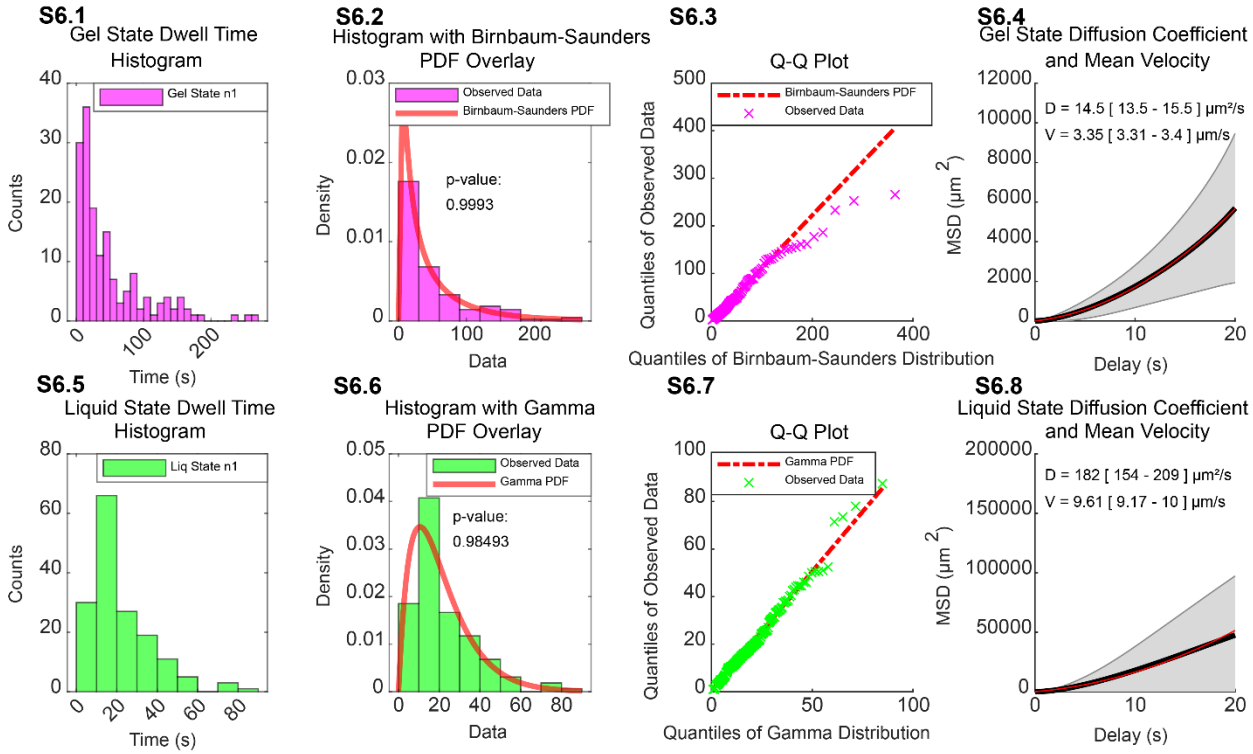

Fig. S6 Gel and Solution State Parameters - Histone H1-488 n2 of 4

Figure S6. Gel and Sol parameters H1-488 n2 of 4
S6.1 Gel state dwell time histogram, showing the frequency of gel state dwell times. S6.2 Gel state dwell Histogram with Birnbaum-Saunders probability density function (PDF) overlay. S6.3 Q-Q plot comparing observed gel state dwell times with the Birnbaum-Saunders distribution. S6.4 Gel state diffusion coefficient (D) and mean velocity (V) derived from MSD analysis. S6.5 Liquid state dwell time histogram, showing the frequency of liquid state dwell times. S6.6 Histogram with Gamma PDF overlay for liquid state dwell times. S6.7 Q-Q plot comparing observed liquid state dwell times with the Gamma distribution. S6.8 Liquid state diffusion coefficient (D) and mean velocity (V) derived from MSD analysis of MSD curves for respective states.

S7.1 H1-488 Microinjection time lapse - n3

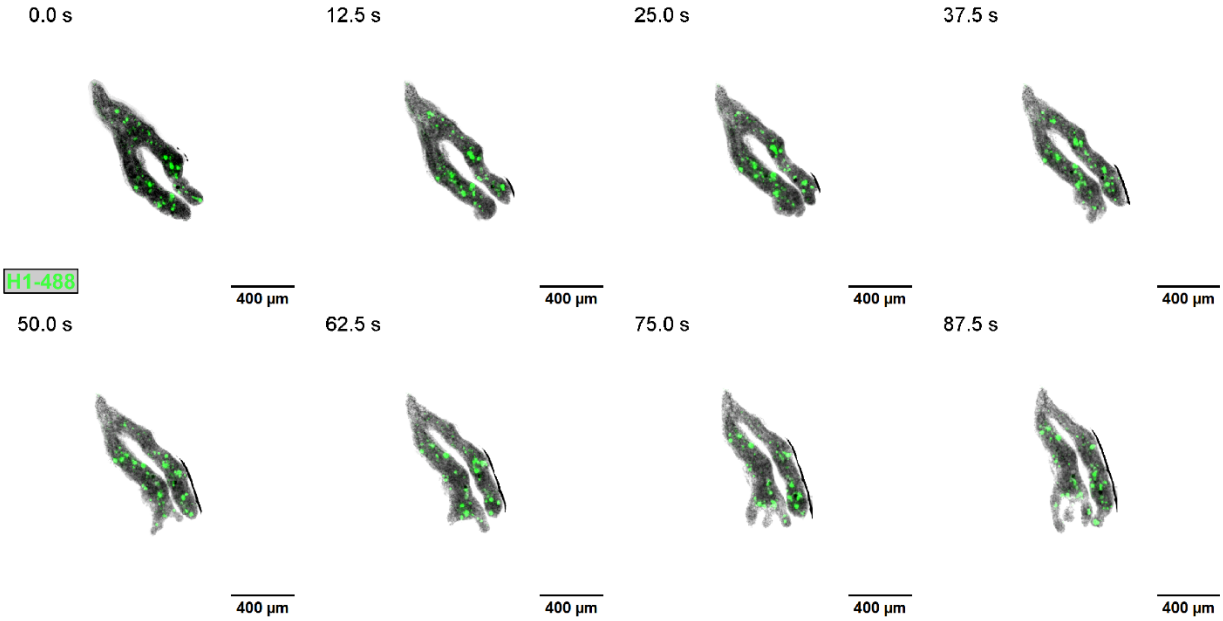

S7.2 Hyper Mixing Simulation - n3

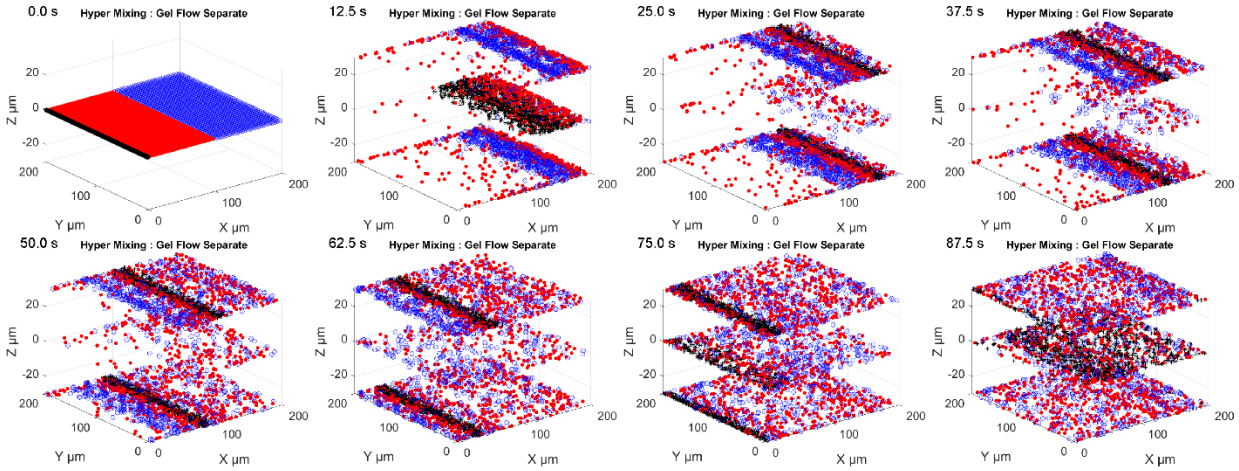

S7.3 Hyper Mixing Simulation Quantification Across Time - n3

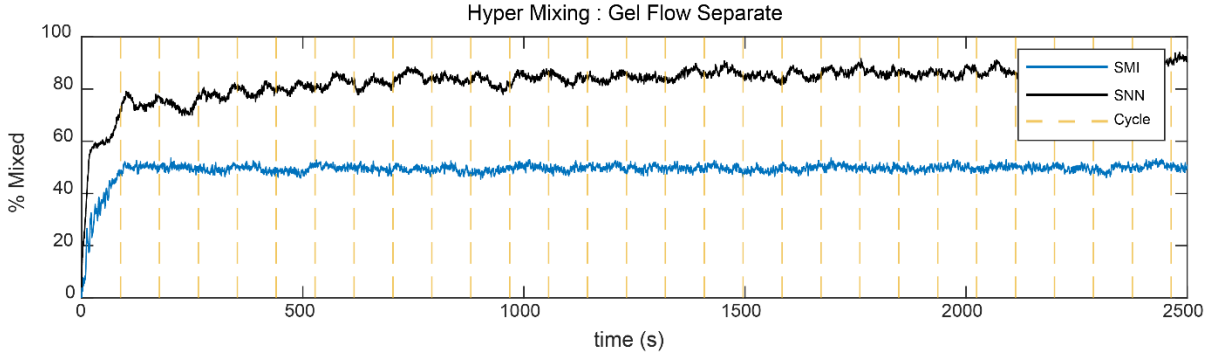

Fig. S7 Mixing of Nuclei - Histone H1-488 n3 of 4

Figure S7. Mixing of Nuclei – Histone H1-488 n3 of 4
S7.1 Fluorescence time lapse panel of histone H1-488. Mean squared displacement (MSD) threshold used to identify gel and liquid state localization in the nuclei labeled with Histone H1-488. Gel (magenta) and liquid (green) bead flow state is represented in the timelapse panel. S7.2 Gel and liquid state hyper-mixing simulation: S7.3 Simulation results of SMI and SNN mixing across time. The plot shows the percentage of mixed nuclei over time, comparing the Subdomain Mixing Index (SMI) and Spatial Nearest Neighbors (SNN) metrics, demonstrating consistent mixing behavior over a 2500-second period.

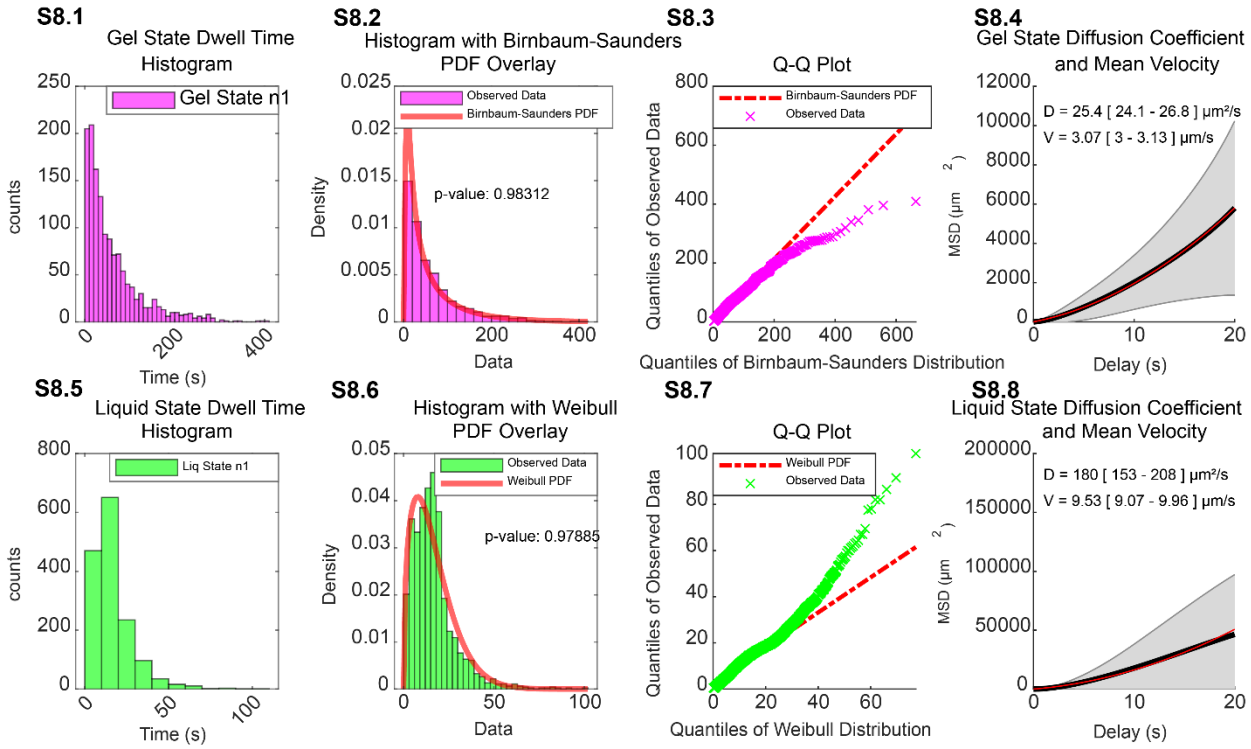

Fig. S8 Gel and Solution State Parameters - Histone H1-488 n3 of 4

Figure S8. Gel and Sol parameters H1-488 n3 of 4
S8.1 Gel state dwell time histogram, showing the frequency of gel state dwell times. S8.2 Histogram with Birnbaum-Saunders probability density function (PDF) overlay for gel state dwell times. S8.3 Q-Q plot comparing observed gel state dwell times with the Birnbaum-Saunders distribution. S8.4 Gel state diffusion coefficient (D) and mean velocity (V) derived from MSD analysis. S8.5 Liquid state dwell time histogram, showing the frequency of liquid state dwell times. S8.6 Histogram with Weibull PDF overlay for liquid state dwell times. S8.7 Q-Q plot comparing observed liquid state dwell times with the Weibull distribution. S8.8 Liquid state diffusion coefficient (D) and mean velocity (V) derived from MSD analysis of MSD curves for respective states.

S9.1 H1-488 Microinjection time lapse - n4

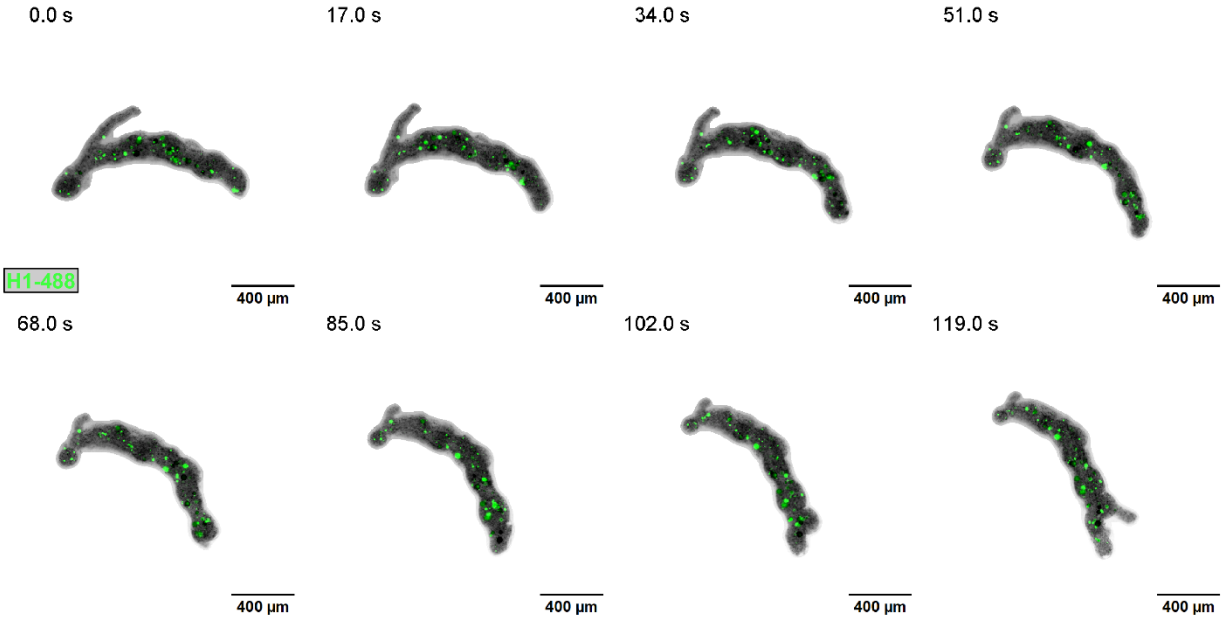

S9.2 Hyper Mixing Simulation - n4

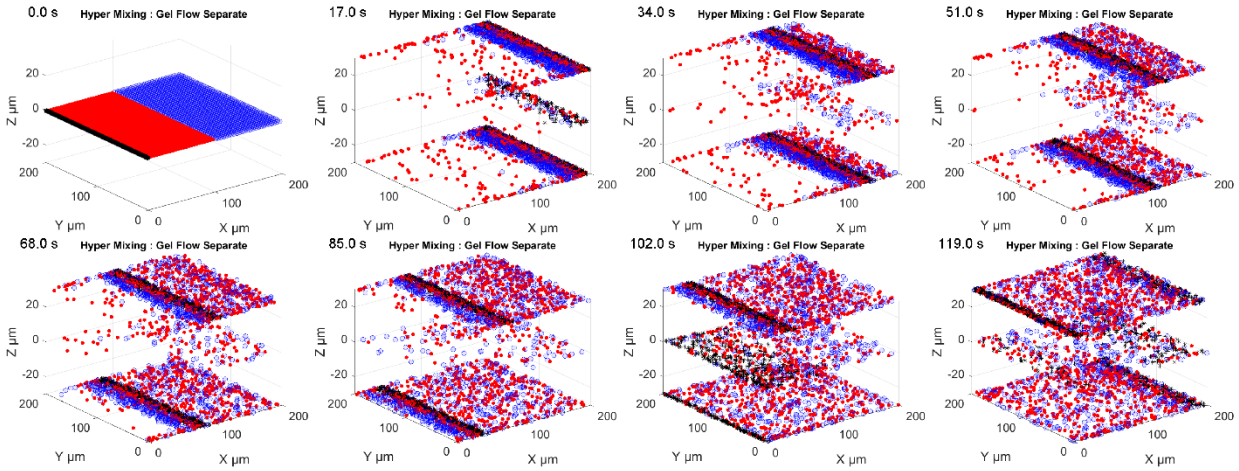

S9.3 Hyper Mixing Simulation Quantification Across Time - n4

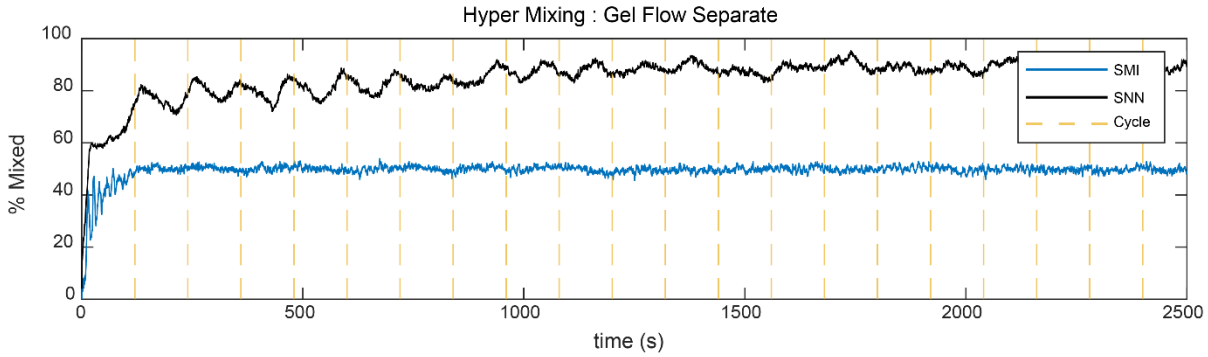

Fig. S9 Mixing of Nuclei - Histone H1-488 n4 of 4

Figure S9. Mixing of Nuclei – Histone H1-488 n4 of 4
S9.1 Fluorescence time lapse panel of histone H1-488. Mean squared displacement (MSD) threshold used to identify gel and liquid state localization in the nuclei labeled with Histone H1-488. Gel (magenta) and liquid (green) bead flow state is represented in the timelapse panel. S9.2 Gel and liquid state hyper-mixing simulation: S9.2 Simulation results of SMI and SNN mixing across time. The plot shows the percentage of mixed nuclei over time, comparing the Subdomain Mixing Index (SMI) and Spatial Nearest Neighbors (SNN) metrics, demonstrating consistent mixing behavior over a 2500-second period.

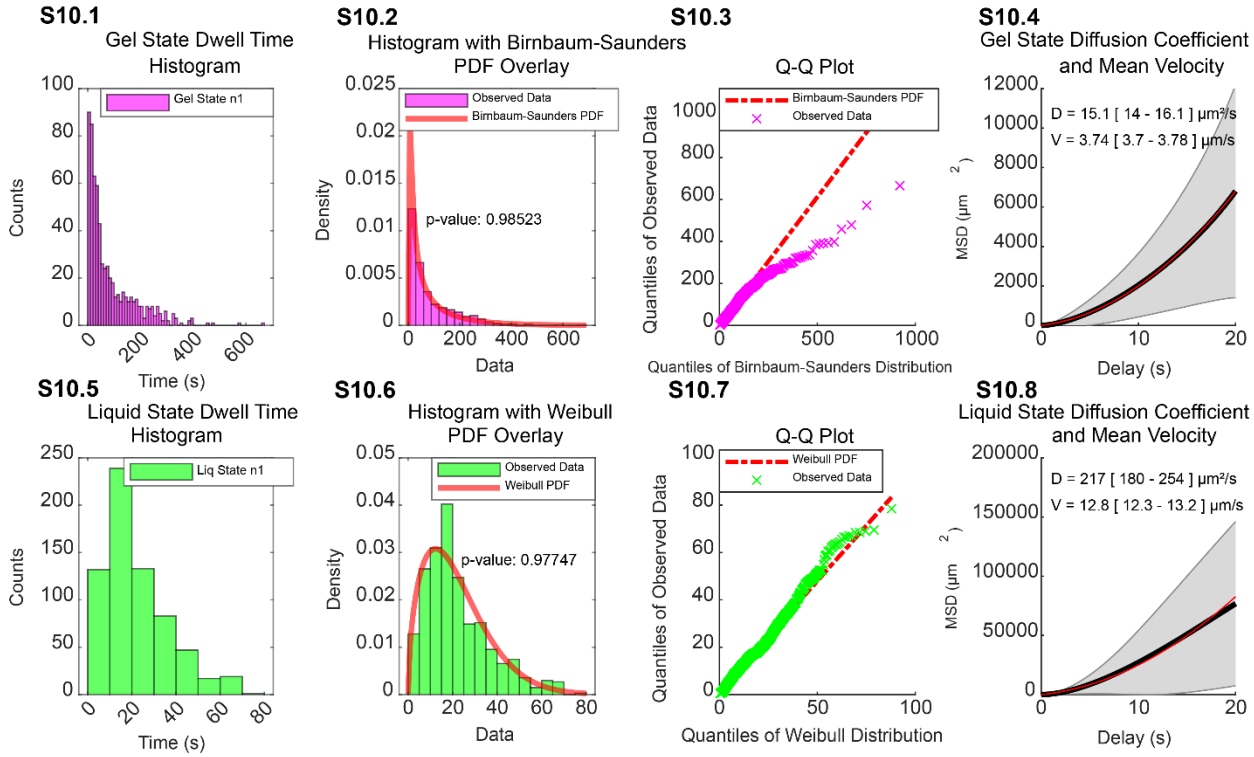

Fig. S10 Gel and Solution State Parameters - Histone H1-488 n4 of 4

Figure S10. Gel and Sol parameters H1-488 n4 of 4
S10.1 Gel state dwell time histogram, showing the frequency of gel state dwell times. S10.2 Gel state dwell Histogram with Birnbaum-Saunders probability density function (PDF) overlay. S10.3 Q-Q plot comparing observed gel state dwell times with the Birnbaum-Saunders distribution. S10.4 Gel state diffusion coefficient (D) and mean velocity (V) derived from MSD analysis. S10.5 Liquid state dwell time histogram, showing the frequency of liquid state dwell times. S10.6 Histogram with Weibull PDF overlay for liquid state dwell times. S10.7 Q-Q plot comparing observed liquid state dwell times with the Weibull distribution. S10.8 Liquid state diffusion coefficient (D) and mean velocity (V) derived from MSD analysis of MSD curves for respective states.

REFERENCES

1) Mullineaux, C. W. (2017). Intracellular diffusion: How bacteria keep proteins moving. eLife, 6. https://doi.org/10.7554/eLife.27074

2) Lu, W., & Gelfand, V. I. (2023). Go with the flow – bulk transport by molecular motors. *Journal of Cell Science*, 136(5), jcs260300. https://doi.org/10.1242/jcs.260300

3) Koslover, E. F., Chan, C. K., & Theriot, J. A. (2017). Cytoplasmic flow and mixing due to deformation of motile cells. *Biophysical Journal*, 113(9), 2077-2087. https://doi.org/10.1016/j.bpj.2017.09.009

4) Domínguez-Martín, E., Hernández-Elvira, M., Vincent, O., Coria, R., & Escalante, R. (2018). Unfolding the Endoplasmic Reticulum of a Social Amoeba: Dictyostelium discoideum as a New Model for the Study of Endoplasmic Reticulum Stress. *Cells*, 7(6), 56. https://doi.org/10.3390/cells7060056

5) Einstein, H. A., & Li, H. (1958). "Secondary currents in straight channels." Proceedings of the American Society of Civil Engineers, 84(2), 1-16.

6) Dimotakis, P. E. (2005). "Turbulent mixing." Annual Review of Fluid Mechanics, 37, 329-356.

7) Stroock, A. D., Dertinger, S. K., Ajdari, A., Mezić, I., Stone, H. A., & Whitesides, G. M. (2002). "Chaotic mixer for microchannels." Science, 295(5555), 647-651.

8) Ottino, J. M., & Wiggins, S. (2004). "Introduction: Mixing in microfluidics." Philosophical Transactions of the Royal Society A: Mathematical, Physical and Engineering Sciences, 362(1818), 923-935.

9) Needleman, D., & Shelley, M. (2019). The stormy fluid dynamics of the living cell. *Physics Today, 72*(9), 32-38. https://doi.org/10.1063/PT.3.4292

10) Smith JJ, Aitchison JD. Peroxisomes take shape. Nat Rev Mol Cell Biol. 2013 Dec;14(12):803-17. doi: 10.1038/nrm3700. PMID: 24263361; PMCID: PMC4060825.

11) Lin, C., Schuster, M., Guimaraes, S. C., Ashwin, P., Schrader, M., Metz, J., Hacker, C., Gurr, S. J., & Steinberg, G. (2016). Active diffusion and microtubule-based transport oppose myosin forces to position organelles in cells. *Nature Communications, 7*, Article 11814. https://doi.org/10.1038/ncomms11814

12) Bandyopadhyay D, Cyphersmith A, Zapata JA, Kim YJ, Payne CK (2014) Lysosome Transport as a Function of Lysosome Diameter. PLoS ONE 9(1): e86847. doi:10.1371/journal.pone.0086847

13) Short, R. B. (1946). Observations on the giant amoeba, Amoeba carolinensis (Wilson, 1900). The Biological Bulletin, 90(1), 8-18. https://doi.org/10.2307/1538058

14) Warren, G. H. (1949). Nuclear and Body Sizes and the Nucleo-Cytoplasmic Ratio in Three Species of Chaos Linnaeus, 1767. *Transactions of the American Microscopical Society*, *68*(1), 34–39. https://doi.org/10.2307/3223203

15) Huysmans, M., & Dassargues, A. (2005). Review of the use of Péclet numbers to represent diffusion and advection dominance in low-permeability environments. Environmental Geology, 47(5), 688–697. https://doi.org/10.1007/s00254-004-1184-4

16) Biello, B., & Sigal, A. (2017). Stability of solutal advective flow in a horizontal shallow layer. Physical Review Fluids, 2(10), 103903. https://doi.org/10.1103/PhysRevFluids.2.103903

17) Meunier, P., & Villermaux, E. (2010). The criterion for chaotic mixing in fluids at high Péclet numbers. Journal of Fluid Mechanics, 662, 134–157. https://doi.org/10.1017/S0022112010003724

18) Ecker, A. (1849). Zur Lehre vom Bau und Leben der contractilen Substanz der niedersten Thiere. Zeitschrift für Wissenschaftliche Zoologie, 1, 218-245.

19) Hyman, L. (1917). Metabolic gradients in Amoeba and their relationships to the mechanism of amoeboid movement. Journal of Experimental Zoology, 24, 55-99.

20) Mast, S. O. (1926). Structure, movement, stimulation, and locomotion in Amoeba. Journal of Morphology, 41, 347-425.

21) Mast, S. O. (1931). Locomotion in Amoeba proteus (Leidy). Protoplasma, 14, 321-330.

22) Mast, S. O. (1934). Amoeboid movement in Pelomyxa palustris (Greeff). Physiological Zoology, 7, 470-478.

23) Allen, R. D. (1961). A New Theory of Ameboid Movement and Protoplasmic Streaming. *Experimental Cell Research*, *Suppl. 8*, 17–31. https://doi.org/10.1016/0014-4827(61)90337-8

24) Shimmen, T., & Yokota, E. (2004). Cytoplasmic streaming in plants. Journal of Plant Research, 117(1), 111-119. https://doi.org/10.1007/s10265-003-0137-1

25) Grebecki, A. (1986). Two-directional pattern of movements on the cell surface of *Amoeba proteus*. *Journal of Cell Science*, 83, 23-35.

26) Wilson, H. V. (1900). Notes on a Species of Pelomyxa. *The American Naturalist*, 34(403), 535-550. https://doi.org/10.1086/277702

27) D. L. Taylor, J. S. Condeelis, P. L. Moore, R. D. Allen; THE CONTRACTILE BASIS OF AMOEBOID MOVEMENT : I. The Chemical Control of Motility in Isolated Cytoplasm . J Cell Biol 1 November 1973; 59 (2): 378–394. doi: https://doi-org.ucsf.idm.oclc.org/10.1083/jcb.59.2.378

28) L W Janson, D L Taylor; In vitro models of tail contraction and cytoplasmic streaming in amoeboid cells.. *J Cell Biol* 15 October 1993; 123 (2): 345–356. doi: https://doi-org.ucsf.idm.oclc.org/10.1083/jcb.123.2.345

29) D L Taylor, Y L Wang, J M Heiple; Contractile basis of ameboid movement. VII. The distribution of fluorescently labeled actin in living amebas.. *J Cell Biol* 1 August 1980; 86 (2): 590–598. doi: https://doi-org.ucsf.idm.oclc.org/10.1083/jcb.86.2.590

30) Comly LT. Microfilaments in Chaos carolinensis. Membrane association, distribution, and heavy meromyosin binding in the glycerinated cell. J Cell Biol. 1973 Jul;58(1):230-7. doi: 10.1083/jcb.58.1.230. PMID: 4125372; PMCID: PMC2109023.

31) RINALDI, R., OPAS, M. and HREBENDA, B. (1975), Contractility of Glycerinated *Amoeba proteus* and *Chaos-chaos**. The Journal of Protozoology, 22: 286-292. https://doi-org.ucsf.idm.oclc.org/10.1111/j.1550-7408.1975.tb05869.x

32) Vivianne T. Nachmias; Further electron microscope studies on fibrillar organization of the ground cytoplasm of chaos chaos. J Cell Biol 1 July 1968; 38 (1): 40–50. doi: https://doi-org.ucsf.idm.oclc.org/10.1083/jcb.38.1.40

33) John S. Condeelis; The self-assembly of synthetic filaments of myosin isolated from Chaos Carolinensis and Amoeba Proteus. J Cell Sci 1 June 1977; 25 (1): 387–402. doi: https://doi.org/10.1242/jcs.25.1.387

34) Pollard TD. The role of actin in the temperature-dependent gelation and contraction of extracts of Acanthamoeba. J Cell Biol. 1976 Mar;68(3):579-601. doi: 10.1083/jcb.68.3.579. PMID: 1030705; PMCID: PMC2109654.

35) Diaz U, Marshall W, Riggs B. Drosophila Embryo Preparation and Microinjection for Live Cell Microscopy Performed using an Automated High Content Analyzer. J Vis Exp. 2021 Jan 19;(167). doi: 10.3791/61589. PMID: 33554960.

36) Tinevez, J.-Y., Perry, N., Schindelin, J., Hoopes, G. M., Reynolds, G. D., Laplantine, E., ... & Eliceiri, K. W. (2017). TrackMate: An open and extensible platform for single-particle tracking. *Methods*, 115, 80-90. https://doi.org/10.1016/j.ymeth.2016.09.016

37) Einstein, A. (1905). On the movement of small particles suspended in stationary liquids required by the molecular-kinetic theory of heat. Annalen der Physik, 322(8), 549-560.

38) Einstein, A. (1928). "Theoretical Observations on the Diffusion of Suspended Particles." *Sitzungsberichte der Preussischen Akademie der Wissenschaften, Physikalisch-Mathematische Klasse*, 1, 235–239.

39) Cho, M., Dutta, P., & Shim, J. (2017). A non-sampling mixing index for multicomponent mixtures. *Powder Technology*, *319*, 434–444. https://doi.org/10.1016/j.powtec.2017.07.011

40) Kadoch, B., Bos, W. J. T., & Schneider, K. (2020). Efficiency of laminar and turbulent mixing in wall-bounded flows. Physical Review E, 101(4), 043104

41) Sirker, J., Pereira, R. G., & Affleck, I. (2009). Diffusion and ballistic transport in one-dimensional quantum systems. Physical Review Letters, 103(21), 216602. https://doi.org/10.1103/PhysRevLett.103.216602

42) Davis, S. H. (1982). Explosive instabilities and breakdown of shock waves. Annual Review of Fluid Mechanics, 14, 15-35.

43) Bouchaud, J. P., & Georges, A. (1990). Anomalous diffusion in disordered media: Statistical mechanisms, models, and physical applications. Physics Reports, 195(4-5), 127-293.

44) Metzler, R., & Klafter, J. (2000). The random walk's guide to anomalous diffusion: A fractional dynamics approach. Physics Reports, 339(1), 1-77. https://doi.org/10.1016/S0370-1573(00)00070-3

45) Zukoski, E. E. (1992). A power-law formulation of laminar flow in short pipes. Journal of Fluids Engineering, 114(4), 601-605. https://doi.org/10.1115/1.2910039

46) Richardson, L. F. (1926). Atmospheric diffusion shown on a distance-neighbour graph. Proceedings of the Royal Society A, 110(756), 709-737. https://doi.org/10.1098/rspa.1926.0043

47) Batchelor, G. K. (1952). Diffusion in a field of homogeneous turbulence II. The relative motion of particles

48) Ottino, J. M. (1989). The Kinematics of Mixing: Stretching, Chaos, and Transport. Cambridge University Press.

49) Pope, S. B. (2000). Turbulent Flows. Cambridge University Press.

50) Zel'dovich, Y. B., Barenblatt, G. I., Librovich, V. B., & Makhviladze, G. M. (1985). The Mathematical Theory of Combustion and Explosions. Consultants Bureau, New York.

51) Allen, R.D. (1983). Amoeboid Movement in Chaos Carolinensis. In: Earnshaw, J.C., Steer, M.W. (eds) The Application of Laser Light Scattering to the Study of Biological Motion. NATO Advanced Science Institutes Series, vol 59. Springer, Boston, MA. https://doi.org/10.1007/978-1-4684-4487-2_34

52) Ottino, J. M. (1989). The Kinematics of Mixing: Stretching, Chaos, and Transport. *Cambridge University Press*.

53) Aref, H. (1990). Mixing of fluid in chaotic flows. *Annual Review of Fluid Mechanics*, 22(1), 345-366. https://doi.org/10.1146/annurev.fl.22.010190.002021

Publishing Agreement

It is the policy of the University to encourage open access and broad distribution of all theses, dissertations, and manuscripts. The Graduate Division will facilitate the distribution of UCSF theses, dissertations, and manuscripts to the UCSF Library for open access and distribution. UCSF will make such theses, dissertations, and manuscripts accessible to the public and will take reasonable steps to preserve these works in perpetuity.

I hereby grant the non-exclusive, perpetual right to The Regents of the University of California to reproduce, publicly display, distribute, preserve, and publish copies of my thesis, dissertation, or manuscript in any form or media, now existing or later derived, including access online for teaching, research, and public service purposes.

DocuSigned by:
Ulises Diaz
B83743E3C95E44B...
Author Signature

11/11/2024
Date